CANCER

Spatiotemporal architecture of immune cells and cancer-associated fibroblasts in high-grade serous ovarian carcinoma

Alexander M. Xu[1,2]*, Marcela Haro[3], Ann E. Walts[4], Ye Hu[5], Joshi John[6,7], Beth Y. Karlan[5,8], Akil Merchant[1,2]†, Sandra Orsulic[5,6,8]†*

High-grade serous ovarian carcinoma (HGSOC), the deadliest form of ovarian cancer, is typically diagnosed after it has metastasized and often relapses after standard-of-care platinum-based chemotherapy, likely due to advanced tumor stage, heterogeneity, and immune evasion and tumor-promoting signaling from the tumor microenvironment. To understand how spatial heterogeneity contributes to HGSOC progression and early relapse, we profiled an HGSOC tissue microarray of patient-matched longitudinal samples from 42 patients. We found spatial patterns associated with early relapse, including changes in T cell localization, malformed tertiary lymphoid structure (TLS)–like aggregates, and increased podoplanin-positive cancer-associated fibroblasts (CAFs). Using spatial features to compartmentalize the tissue, we found that plasma cells distribute in two different compartments associated with TLS-like aggregates and CAFs, and these distinct microenvironments may account for the conflicting reports about the role of plasma cells in HGSOC prognosis.

INTRODUCTION

The most common and most lethal subtype of ovarian cancer is high-grade serous ovarian carcinoma (HGSOC) (*1*). Standard treatment for HGSOC combines surgical cytoreduction with platinum-based chemotherapy. Typically, this treatment is initially successful in achieving remission, but cancer recurs in the vast majority of cases. Although these patients with recurrent disease might respond to additional cycles of chemotherapy, most ultimately develop resistance. To modulate resistance, immune cells can promote and/or inhibit tumor progression depending on signals received from the tumor microenvironment. In particular, cancer-associated fibroblasts (CAFs) are emerging as critical regulators of immune cell activity and tumor development, mediated by proteins such as fibroblast activation protein (FAP) (*2*–*4*) and podoplanin (PDPN) (*5*, *6*). Multiple studies have reported an uneven distribution of different immune cell types and/or different maturation stages of the same cell type across different tumors and even within the same tumor. These observations provided the basis for the development of "immunoscores" as predictors of survival, metastasis, and therapeutic response (*7*–*15*).

In primary HGSOC, longer survival has been associated with tumor-infiltrating $CD8^+$ T cells (*16*–*18*) and plasma cells in tertiary lymphoid structures (TLSs). On the basis of the presence and distribution of $CD8^+$ T cells in ovarian cancer, three main spatial patterns have been described: infiltrated, excluded, and desert (*19*, *20*). While desert tumors consist primarily of epithelial cells and are largely devoid of immune cells, infiltrated tumors have abundant immune infiltrates evenly distributed in cancer and stromal areas. Excluded tumors typically exhibit a higher CAF content than the infiltrated and desert tumors and the majority of T cells present are not in direct contact with cancer cells. Excluded tumors are associated with poor survival although it is unclear if this is due to dysfunctional T cells sequestered in the tumor stroma or limited access to chemotherapy due to the dense extracellular matrix (ECM) secreted by CAFs (*20*). While immune cell distribution and function have been extensively studied in primary tumors, less is known about the distribution of immune cell subsets during tumor progression and chemotherapy resistance. In a mouse model of ovarian cancer, it has been shown that cancer progression is primarily driven by a switch from immunoproficient to immunosuppressive immune cell types rather than by a loss of tumor immunogenicity (*21*). It is currently unknown how this equilibrium is established and how the ratios and spatial distribution of different stromal cell types affect tumor progression and response to therapy.

Ratios between different cell types in a tumor, including cancer cells, fibroblasts, and immune cells, can be studied in detail with single-cell RNA sequencing (RNA-seq) analyses. Single-cell transcriptomic studies in ovarian cancer have contributed much to our understanding of HGSOC; however, most of the studies were done using samples from a small number of patients. Olalekan *et al.* (*22*) analyzed omental metastases from six patients with ovarian cancer, of which four were HGSOC. Izar *et al.* (*23*) analyzed single-cell transcriptomes in ascites from 11 patients with HGSOC. Although Pietilä *et al.* (*24*) conducted RNA-seq expression analysis of primary, metastatic, and recurrent ovarian cancer from 32 patients, they focused on genes involved in ECM remodeling. Using RNA-seq analysis, Kreuzinger *et al.* (*25*) compared patient-matched primary and recurrent fresh-frozen tissue samples from 66 patients with HGSOC

[1]Board of Governors Regenerative Medicine Institute, Cedars-Sinai Medical Center, Los Angeles, CA 90048, USA. [2]Division of Hematology and Cellular Therapy, Samuel Oschin Comprehensive Cancer Institute, Cedars-Sinai Medical Center, Los Angeles, CA 90048, USA. [3]Department of Obstetrics and Gynecology and Samuel Oschin Comprehensive Cancer Institute, Cedars-Sinai Medical Center, Los Angeles, CA 90048, USA. [4]Department of Pathology and Laboratory Medicine, Cedars-Sinai Medical Center, Los Angeles, CA 90048, USA. [5]Department of Obstetrics and Gynecology, David Geffen School of Medicine, University of California Los Angeles, Los Angeles, CA 90095, USA. [6]Department of Veterans Affairs, Greater Los Angeles Healthcare System, Los Angeles, CA 90073, USA. [7]Department of Medicine, Division of Geriatrics, David Geffen School of Medicine, University of California Los Angeles, Los Angeles, CA 90095, USA. [8]Jonsson Comprehensive Cancer Center, University of California Los Angeles, Los Angeles, CA 90095, USA.
*Corresponding author. Email: alexander.xu@cshs.org (A.M.X.); sorsulic@mednet.ucla.edu (S.O.)
†These authors contributed equally to this work.

and found that the tumor microenvironment was a major contributor to the differential gene expression. Using gene expression profiles and immunohistochemistry (IHC) analyses of formalin-fixed paraffin-embedded (FFPE) samples, Westergaard *et al.* (*26*) investigated the molecular features of matched primary and recurrent HGSOC from nine patients and found that gene signatures of fibroblasts and immune cells were often expressed at higher levels in recurrent tumors. While these studies showed the heterogeneity of HGSOC, they did not focus on the spatial relationships between cell types and tissue architecture.

More recently, spatial resolution has been added to single-cell analysis. Commercially available tools for highly multiplexed spatial protein analysis include imaging mass cytometry (IMC) (*27*), multiplexed ion beam imaging (*28*), and CO-Detection by indEXing (CODEX) (*29*). When applied to tumor studies, these spatially resolved methods can provide an added layer of spatial context by describing the microenvironmental niches where each cell type can be found (*29*, *30*). This is essential for clinical translation, as molecular analysis (e.g., RNA-seq) is relatively costly and imaging remains the most common modality for biomarkers and clinical decision-making. Whereas typical biomarkers focus on cellular composition as percentages and qualitative expression levels (*31*), automated quantification of more complex cell patterns within tissue, such as tissue interfaces and cell-cell interactions, is still in its infancy in pathology. These spatial patterns represent the dynamic biology of tumors (*16*, *32*) and have shown promise as more accurate biomarkers, but spatial analysis has not yet been widely applied in ovarian cancer and the studies published to date were conducted on small numbers of samples. An IMC analysis of pre- and on-treatment immune therapy biopsy samples from six patients showed that treatment response correlated with an increase in $CD8^+$ T cells and $FoxP3^+$ cells (*33*). In addition, an IMC study of primary HGSOC from 20 short-term [overall survival (OS), ≤20 months] and 21 long-term (OS, ≥80 months) patients showed different densities of $Granzyme^+$ $CD8^+$ cytotoxic T cells, $CD45RO^+$ $CD4^+$ memory T cells, $B7^+H4^+$ $Keratin^+$ tumor cells, two subtypes of $CD73^+$ fibroblasts, and a subset of $CD31^+$ endothelial cells in tumors from the two patient groups (*34*). A spatially resolved transcriptomic analysis of 12 patients with HGSOC with different responses to neoadjuvant chemotherapy emphasized the importance of stromal signaling and immune cell localization (*35*).

Currently, the costs associated with advanced spatial imaging tools and computational methods, including machine infrastructure, computational power, and bioinformatics expertise, stifle clinical translation (*36*). Bridging the gap between developing technologies such as IMC and traditional methods of clinical oncology presents a major challenge in the modern single-cell omics era (*37*). The clinical analogs to IMC are IHC, which is limited to a few markers but can be performed quickly and inexpensively, and hematoxylin and eosin (H&E), which capture a wide range of interpretable histological features. In ovarian cancer, multiplex IHC has been used to correlate patient outcomes and tumor molecular characteristics with the distribution of major immune cell subtypes, including T cells, B cells, and plasma cells (*38*). Here, we show that IMC not only reproduces equivalent histologic analyses but also generates deeper insights using the additional protein markers available. We used IMC to perform deep phenotyping and spatial analysis of patient-matched primary, synchronous metastatic, and post-platinum–based chemotherapy HGSOC recurrence samples from 42 patients. This study represents the largest collection of highly multiplexed, spatially resolved imaging data in HGSOC to date. We identified quantifiable spatial protein features of lymphocytes and fibroblasts associated with early relapse (≤15 months after primary optimal debulking), including architectural changes between primary, recurrent, and metastatic sites. Further genetic and protein spatial analysis found that B cells and plasma cells are spatially segregated with respect to PDPN-expressing CAFs in early relapse patients, and we propose a hypothetical mechanism driving this spatial prognostic biomarker.

RESULTS

Imaging mass cytometry reveals single-cell heterogeneity of ovarian cancer

We generated a tissue microarray (TMA) with de-identified FFPE patient tissue samples comprising up to triplicate 1-mm cores of patient-matched primary HGSOC, synchronous pretreatment metastasis, and metachronous posttreatment/recurrent metastasis samples (hereafter referred to as "primary," "synchronous metastasis," and "recurrence," respectively) from 42 optimally debulked patients with HGSOC who recurred during or after platinum-based chemotherapy (Fig. 1A and table S1). The time to recurrence ranged from 5.5 to 51.7 months after primary debulking surgery. Of the 42 patients, 16 recurred within 15 months following optimal primary debulking surgery, which we categorized as "early relapse." The remaining 26 patients were categorized as "late relapse" (Fig. 1A). We used IMC analysis of the TMA to study the temporal evolution of spatial tumor architecture.

We performed IMC using an immune-centric panel of 38 markers (Fig. 1B and table S2), finding cell heterogeneity across all regions of interest (ROIs) analyzed. Initially, major cell phenotyping markers were identified and used for PhenoGraph clustering (Fig. 1C), identifying three primary cell categories: immune cells (combined lymphoid and myeloid immune cell lineages), fibroblasts, and epithelial cancer cells. In addition to interpatient heterogeneity in cell composition (fig. S1A), we observed heterogeneity across tumor sample types—primary, synchronous metastatic, and recurrent (Fig. 1D; stacked bar plot to show summation to 1, error bars denote SD; fig. S1B shows the underlying distribution). We observed more epithelial cells and fewer immune cells in primary than synchronous metastatic and recurrent tumors, but the difference was not statistically significant. A significant increase in immune cells was observed in tumors collected from lymph nodes, suggesting that the surrounding tissue influenced the analysis (Fig. 1E and fig. S1C). We observed more fibroblasts and fewer cancer epithelial and immune cells in ROIs from patients with early relapse ($n = 16$) than those from patients with late relapse ($n = 26$), but these differences were not statistically significant (Fig. 1F and fig. S1D). No significant differences in cell proportions were observed by age, stage, grade, ethnicity, or BRCA1/2 mutation status.

Highly multiplexed IMC performs phenotyping of immune and fibroblast subsets

Next, we performed fine-grained phenotyping of immune cells, identifying B cells ($CD19^+$ or $CD20^+$), plasma cells ($CD138^+/CD27^+/CD38^+$), T cells ($CD3^+/CD4^+$ or $CD8^+$), and macrophages and myeloid cells ($CD68^+$ and $CD11b^+$) (Fig. 2, A and B). T cells were further subdivided into $CD4^+$, $CD8^+$, and regulatory T (T_{reg}) ($CD4^+/FoxP3^+$) cells (fig. S2, A to C; error bars denote SD). Fibroblasts were further subdivided by PhenoGraph and labeled by expression of FAP,

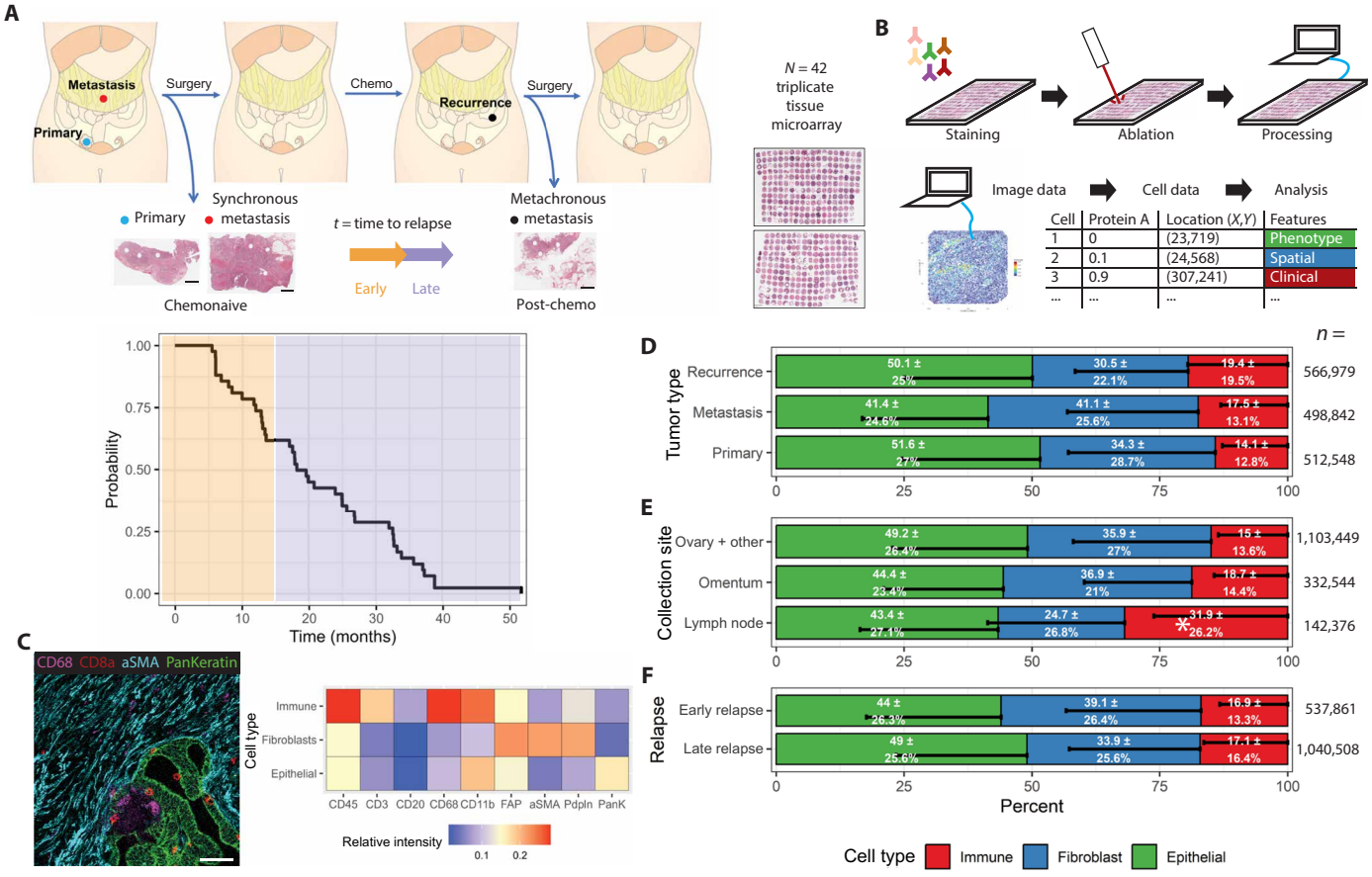

Fig. 1. IMC experimental methods and phenotyping. (**A**) Patient-matched primary, synchronous metastasis, and recurrent metastasis HGSOC samples from 42 patients were assembled into a TMA. The Kaplan-Meier survival curve below shows the time to relapse, with patients classified as early or late relapse (<15 or >15 months to relapse, respectively). Scale bars, 4 mm. (**B**) Imaging mass cytometry was performed by staining the tissue with metal ion–tagged antibodies, ablating the tissue, and performing image data analysis. (**C**) Three major cell types and their protein expression patterns are shown in sample IMC images and a heatmap: immune cells, fibroblasts, and epithelial (cancer) cells. Scale bar, 25 μm. (**D**) Cell composition of (regions of interest) ROIs was approximately 50 to 55% epithelial cancer cells, 25 to 30% fibroblasts, and 15 to 20% immune cells in primary, synchronous metastasis, and recurrence tumor types. (**E**) Lymph node metastases contained elevated levels of immune cells, $P = 1.1 \times 10^{-5}$, analysis of variance (ANOVA). (**F**) Early and late relapse conditions were associated with similar proportions of immune cells, fibroblasts, and epithelial cells. Stacked bar plots are shown to illustrate the summation to 1, error bars denote SD, and the error bar is single-sided to reduce visual clutter. Cell proportion differences are not statistically significant by ANOVA unless noted with *.

α–smooth muscle actin (α-SMA), and PDPN, or any combination of the three markers, to represent different fibroblast subtypes (Fig. 2C). Clustering of ROIs by their cell proportions identified an immune-dominant cluster (cluster 7) and a range of fibroblast- to epithelial-dominated clusters (fig. S2D).

Within the immune compartment, macrophages comprised ~45% of all immune cells, while other myeloid cells comprised ~21% (Fig. 2D; error bars denote SD). Different T cell subtypes were identified, including $CD4^+$, $CD8^+$, T_{reg}, CD4/CD8 double-positive, and $CD20^+$ T cells (*39, 40*). CD4/CD8 double-positive and $CD20^+$ T cells (fig. S2E) may represent densely packed T and B cells that were not separated by segmentation, although both CD4/CD8 double-positive and $CD20^+$ T cells have been implicated in various cancers including ovarian (*40–45*). Plasma cells were difficult to define due to high CD138 expression in non-immune cells, such as epithelial tumor cells (*41*). Clusters were manually curated and validated by H&E. We reclassified a subset of $CD11b^+$ cells from immune to epithelial cells as CD11b was expressed at high levels in a subset of epithelial cancer cells (fig. S2F) as previously observed by immunofluorescence and flow cytometry (*42*). The most common fibroblast cluster expressed FAP, α-SMA, and PDPN, and fibroblasts expressing each combination of these markers were recorded (Fig. 2E; error bars denote SD). Ki67, a marker of proliferation, was expressed at high levels in epithelial cells; moderate levels in T and B lymphocytes; and low levels in macrophages, myeloid cells, and fibroblasts (fig. S2G).

Patients presented a diversity of immune and fibroblast cell type distributions depending on the cell and tumor type (fig. S2H). Considering all cells, the proportion of T cells significantly increased from primary to recurrence samples ($P = 0.0038$, Tukey's HSD) but not primary to metastasis ($P = 0.33$), confirming previously reported results (*26*, *43*). As expected, tumors collected from lymph nodes had elevated lymphocyte numbers due to the tumor-surrounding tissue (fig. S2C). Among fibroblasts, metastatic tumors had fewer $\alpha\text{-SMA}^+$ fibroblasts (metastasis to primary/recurrence, $P = 0.045/0.028$), and recurrent tumors had fewer triple-positive fibroblasts (metastasis to recurrence, $P = 0.0024$). Immune proportions were heterogeneous

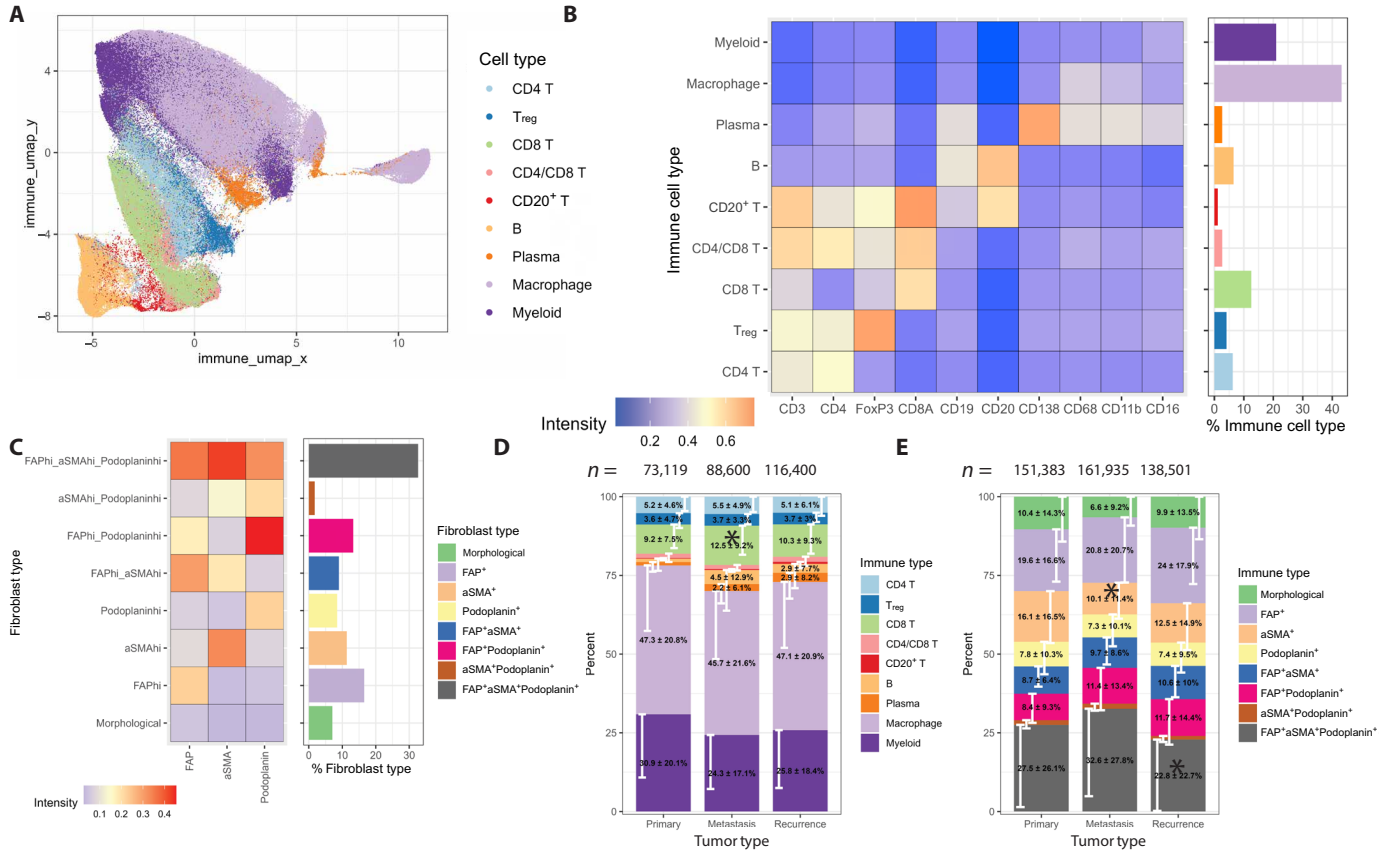

Fig. 2. Fine-grained phenotyping. (**A**) Major immune cell types are plotted after applying Uniform Manifold Approximation and Projection (UMAP). Nine distinct immune subtypes were categorized. (**B**) The relative proportion and average expression pattern of immune subtypes are shown, identified by positive and negative selection. (**C**) Fibroblast subtypes categorized by the relative expression level of up to three markers—FAP, α–smooth muscle actin (α-SMA), and PDPN—are shown, along with their proportions. (**D** and **E**) Relative proportions of immune subtypes (D) and fibroblast subtypes (E) are shown for each tumor type. CD8 T cells as a fraction of immune cells were observed at significantly higher proportions in metastasis samples than primary samples; $P = 0.028$, Tukey's test. Stacked bar plots are shown to illustrate the summation to 1, error bars denote SD, and the error bar is single-sided to avoid visual clutter. Cell proportion differences were not statistically significant by ANOVA unless noted with *.

among patients, due in part to concentrated lymphocyte-rich areas (lymphoid aggregates; fig. S2H).

Spatial analysis elucidates microenvironmental heterogeneity of HGSOC

To better characterize the spatial heterogeneity, we first analyzed the spatial distribution of major cell types—immune cells, fibroblasts, and epithelial cancer cells—across entire ROIs. We used a method called ΔGcross analysis, which is used to study how cell types spatially colocalize (*44*–*46*). Here, positive ΔGcross indicates that two cell types are separated and negative ΔGcross indicates close contact and mixing (fig. S3A). For example, in a representative ROI, well-separated epithelial and fibroblast regions create a distinctive pattern of ΔGcross measurements (Fig. 3A). After clustering using the average ΔGcross values for each ROI between immune cell, fibroblast, and epithelial cell distances, nine clusters of spatial organization were observed (Fig. 3B). Tissue patterns emerge from this clustering, such as ROIs with isolated immune or epithelial areas, or periodic patterns. Primary tumors were enriched in fibroblast-isolated ROIs, and recurrent tumors were enriched in periodic structures and depleted in dispersed tumors (fig. S3B). Immune-isolated ROIs were rare but enriched in samples of lymph node metastases (fig. S3C). These spatially informed clusters are distinct from the clusters generated by cell type proportions only (fig. S3D) which demonstrates that tissue morphology can be quantified and that cell type proportions alone are insufficient to capture morphology. We followed this sample-level ΔGcross analysis with finer-grained single-cell level spatial analyses to resolve details of spatial heterogeneity.

We used spatial analysis to identify TLS-like lymphoid aggregates, which have been associated with improved survival in ovarian cancer (*47*). Histologically, a TLS is defined as a lymphoid aggregate that contains a germinal center and high endothelial venules (*48*); however, these criteria may be absent in thin histologic slices used for IMC. Since lymphoid aggregates are known to be enriched for T and B cells and depleted of epithelial cancer cells, we defined lymphoid aggregates by a spatial analysis strategy that calculates a spatial enrichment score that reflects local cell concentrations or "density" at the single-cell level (Fig. 3C) (*49*). A lymphoid aggregate was defined by first identifying cells with combined T and B cell enrichment scores >1 and epithelial enrichment scores <0.8 (Fig. 3D). All cells satisfying these conditions were passed through a connectivity and size filter (>50 cells less than 15 μm apart from each other) resulting

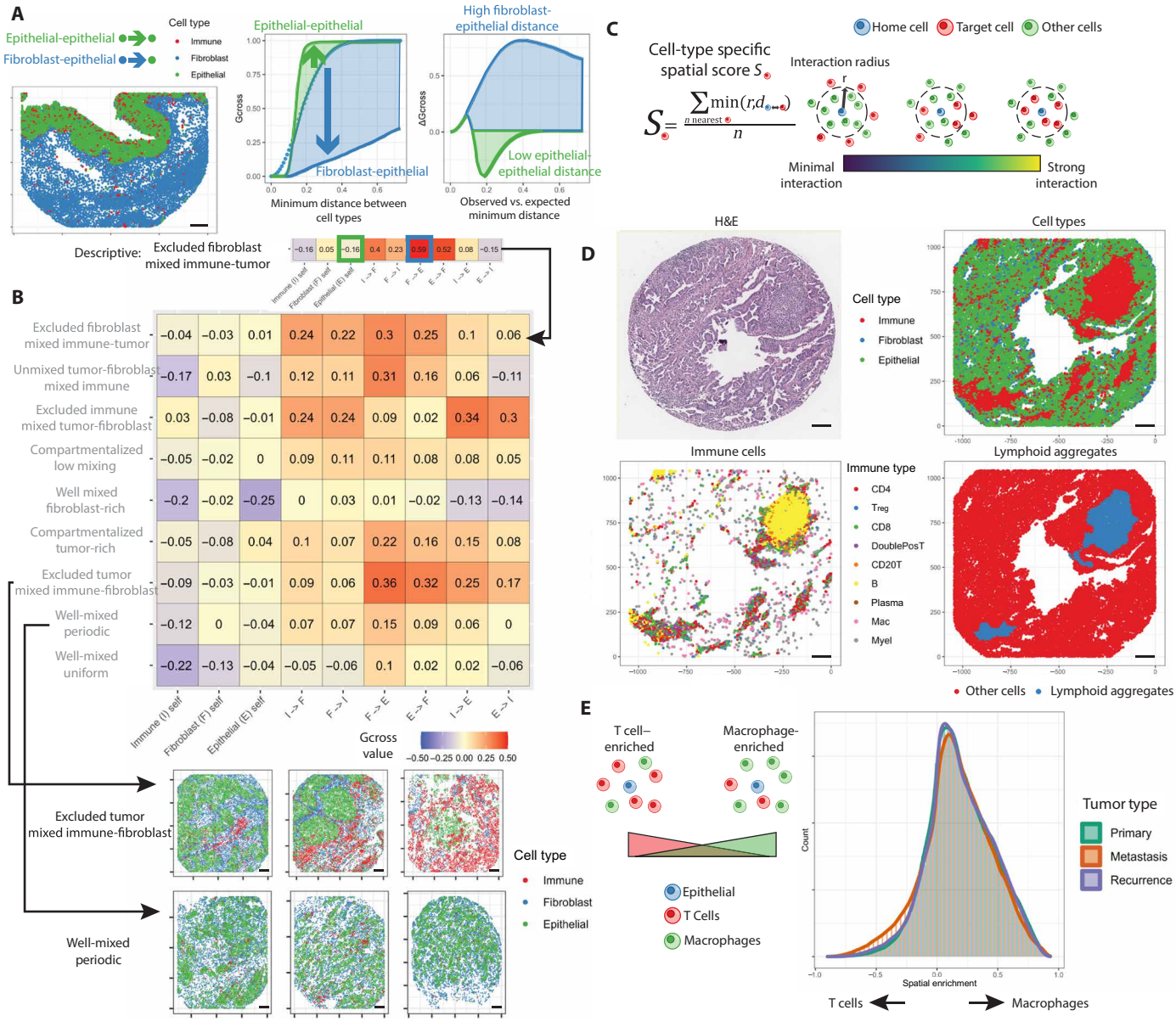

Fig. 3. IMC spatial analysis. (**A**) For a sample image colored by cell type, Gcross analysis generated a cumulative distribution function of minimum cell-cell distances, and ΔGcross calculated the mean difference between the observed and expected cell-cell distances. High fibroblast-epithelial separation and low epithelial-epithelial separation are highlighted in blue and green, respectively. (**B**) A heatmap of clusters generated by ΔGcross comparisons shows manually annotated spatial patterns. Examples of ROIs in cluster 3 (immune-excluded tumors) and cluster 2 (well-mixed cells) are shown. (**C**) The spatial relationship of cells to other cell types was calculated by measuring the distance to five nearest neighbors, truncating the distance at 100 μm, and measuring the average of the five distances. (**D**) Spatial analysis of a sample IMC image shows immune cells, subtypes, and a lymphoid aggregate. (**E**) Single-cell spatial biases for T cells versus macrophages were calculated for each cell. Epithelial cells in synchronous metastatic tumors showed an increase in spatial T cell bias relative to other tumor types ($P < 1 \times 10^{-15}$, Tukey's test), and recurrence tumors showed a smaller spatial T cell bias relative to primary tumors ($P = 8.7 \times 10^{-5}$, Tukey's test). All scale bars, 100 μm.

in the detection of 93 lymphoid aggregates containing 569 ± 1409 cells on average.

Using the spatial enrichment scores, we explored the composition of immune cells in different areas of the tumors with more emphasis on the local microenvironment than the ΔGcross analysis. Lymphoid aggregates were the most prominent, well-defined collections of cells. Primarily composed of T cells and B cells, lymphoid aggregates had similar macrophage density to other stromal tissue, and lower tumor and fibroblast density (fig. S3E). The immune composition in either epithelial-enriched or fibroblast-enriched areas was similar (fig. S3F). We compared the relative spatial enrichment of macrophages versus T cells relative to epithelial cells, finding that epithelial cells in metastatic tumors were relatively enriched in T cells versus macrophages, despite the lower proportion of T cells than in recurrence tumors (primary to metastasis and recurrence to metastasis, $P < 1 \times 10^{-16}$, primary to recurrence, $P = 8.7 \times 10^{-5}$, Tukey's test; Fig. 3E).

Spatially defined cell patterns associate with early relapse

We studied whether the severity of the disease, as measured by time to relapse (<15 or >15 months), was significantly associated with tissue composition. Considering different tumor types independently (primary, metastatic, and recurrent), no differences in cell percentages of fibroblasts, immune cells, epithelial cells, or immune cell subtypes were significantly associated with early relapse (fig. S4A). By proportion of cell composition clusters (fig. S2D), early relapse ROIs were statistically different than late relapse ROIs ($P = 0.023$, chi-square test; fig. S4B), with an increase in an FAP/α-SMA/PDPN-enriched fibroblast cluster. No ΔGcross spatial clusters were associated with early relapse ($P = 0.72$; fig. S4C). Modeling the relationship of cell proportion measurements in entire ROIs with early relapse yielded two significant results associated with early relapse—the proportion of fibroblasts that were $PDPN^+$, and the proportion of FAP^+ $\alpha\text{-}SMA^+$ $PDPN^+$ triple-positive fibroblasts ($q < 0.05$; fig. S4D). When primary, metastasis, and recurrence samples were analyzed individually, the fibroblast populations were found to be most significantly different in recurrence samples, while $CD4^+$ T cells were significantly associated with early relapse in primary tumors only (fig. S4E).

We hypothesized that the spatial heterogeneity of tissue was conflated with cell proportion measurements and that spatially informed analysis of immune, fibroblast, and epithelial cancer cell composition would provide more relevant or significant relationships with early relapse status. We first observed that in early relapse patients, epithelial cells were more spatially enriched for macrophages versus T cells ($P < 1 \times 10^{-16}$, *t* test; fig. S4F), suggesting that cellular-level spatial analysis reveals differences where the overall composition of tissue does not. Then, we used the same spatial metrics used to define lymphoid aggregates to perform a "digital cell biopsy" by selecting subsets of tissue to compare between patients, specifically the immune-, fibroblast-, and epithelial-enriched zones. This allows for more effective "like versus like" comparisons between each ROI and addresses potential biases introduced by sampling tissue for TMA construction. Isolation of immune-, fibroblast-, and epithelial-enriched zones was performed using either a nearest neighbor or spatial enrichment threshold (Fig. 4A, epithelial example), with the nearest neighbor strategy used to separate regions surrounding isolated epithelial tumor cells versus dense tumor areas (Fig. 4B). Among all cell proportions measured in either immune-, fibroblast-, or epithelial-enriched digital cell biopsies, fibroblast-related metrics were the most significant terms after multi-test correction (Fig. 4C). A significant reduction in epithelial cancer cells and increases in fibroblasts in fibroblast-enriched zones were observed in early relapse patients (Fig. 4D). Compared to previous ROI-level metrics (fig. S4D), the spatial biopsy method identified the specific areas of the tissue where the most changes were observed between patients with early and late relapse.

Fewer lymphoid aggregates were detected in early relapse patients, with an average of 1.56 lymphoid aggregates in early relapse ROIs and 1.91 in late relapse ROIs. Lymphoid aggregates also appeared to be smaller in early relapse patients (418 ± 619 versus. 635 ± 1636 cells). Overall, lymphoid aggregates appeared in 52 out of 262 ROIs. After removing samples taken from lymph node metastases, lymphoid aggregates were detected in 38 of the remaining ROIs. ROIs from patients with early relapse averaged 1.42 aggregates (240 ± 191 cells) while ROIs from patients with late relapse averaged 1.83 (300 ± 634 cells). Since the lymphoid aggregates encompassed 73% of all B cells and 26% of all T cells, we analyzed the immune composition of ROIs outside of lymphoid aggregates to explore the contributions of more isolated, infiltrating immune cells. After comparing the significance of cell proportion comparisons with and without lymphoid aggregates, the fibroblast-associated significant associations remained significant, while other immune-related terms increased in significance but remained below the $q < 0.05$ threshold (fig. S4G).

We next considered the change in cellular composition between tumor types within patients to explore the spatiotemporal dimension of ovarian cancers. We hypothesized that the composition of different tumor types from the same patient could change by early relapse status. After measuring the change in each patient's tumor composition between tumor types (primary, synchronous metastasis, and recurrence) with whole ROI-level metrics such as the total T cell percentage, we observed no significant changes. However, in all three digital biopsies, immune-enriched, fibroblast-enriched, and epithelial-enriched, we observed immune and fibroblast populations that were significantly associated with early relapse (Fig. 4E). These populations changed between tumor types within each patient according to the relapse status. For example, B cell percentages in fibroblast-enriched areas were greater in recurrent than primary tumors for late relapse patients, but the reverse trend was observed in early relapse patients (Fig. 4F).

$PDPN^+$ CAFs are associated with malformed lymphoid aggregates enriched in plasma cells

The digital biopsies in IMC unveiled a significant correlation between early recurrence in HGSOC and the aberrant spatial organization of TLS-like lymphoid aggregates and CAFs. Building upon this finding, we used IHC and digital spatial profiling techniques to differentiate immune cell infiltrates between TLS-like lymphoid aggregates and CAFs. We focused on $PDPN^+$ CAFs, which have been associated with poor outcomes in multiple cancer types, including ovarian cancer (*50*–*53*). Consistent with previous reports, IHC staining of the TMA showed PDPN expression in endothelial cells of lymphatic vessels (*50*), fibroblastic reticular cells (FRCs) (fig. S5A, inset) (*6*, *51*), and CAFs (*52*–*58*). $PDPN^+$ CAFs were frequently associated with partially organized immune cells that resembled TLS but lacked germinal centers (fig. S5B, inset). These malformed lymphoid aggregates had sparse $CD20^+$ B cells yet abundant $CD79A^+$ $BOB.1^+$ $CD19^{weak}$ $CD38^+$ B cells, which likely represent plasma cells.

To elucidate the molecular features of lymphoid infiltrates, GeoMx digital spatial profiling with whole genome RNA-seq to measure the differential spatial expression of 11,470 genes. We selected seven ROIs adjacent to immune infiltrates in PDPN-negative areas (total, 5781 nuclei; ROI range, 183 to 1413 nuclei) and seven ROIs in immune infiltrates in PDPN-positive areas (total, 2346 nuclei; ROI range, 200 to 655 nuclei) (Fig. 5A). Selection criteria for ROIs included the presence of more than 150 nuclei in a polygonal selection, the existence of an immune infiltrate, and the presence or absence of PDPN expression in an adjacent slide stained via multiplex immunofluorescence (mIF) with PDPN, CD19, CD20, and CD38 antibodies. We determined first that B cell– and plasma cell–related genes were spatially differentially expressed. Among significant genes with at least 25% differential expression between PDPN-positive or -negative areas, functional annotation with the Database for Annotation, Visualization and Integrated Discovery (DAVID) (*59*) revealed enrichment of the Gene Ontology term for IgG immunoglobulin complex (genes: IGHG4, IGHG1, IGKC, $q = 7 \times 10^{-4}$, Fisher's exact test, Benjamini-Hochberg correction; tables S3 and S4). Possibly due to limited ROIs and sample heterogeneity, PDPN was expressed at higher levels in

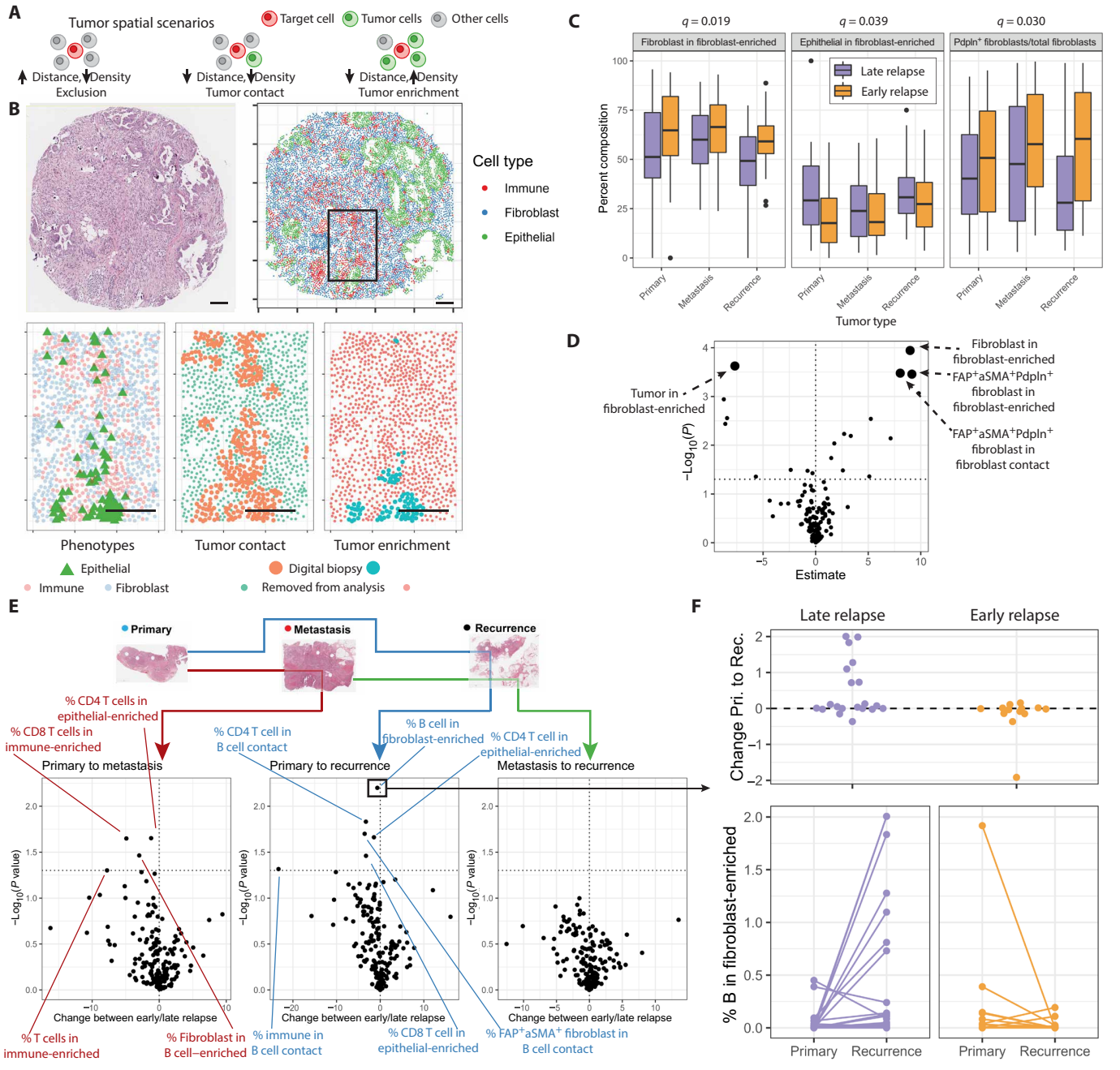

Fig. 4. Spatial analysis of early and late relapse patients. (**A**) A spatial strategy was used to obtain "digital cell biopsies" that excise specific zones of each tumor. For example, two types of biopsies were generated for tumor cells to separate cells with no tumor contact (left), from cells with any tumor contact (middle), and cells in tumor-enriched areas (right). (**B**) In the image shown (IHC, top left; IMC phenotypes, top right), digital biopsies isolated different spatial regions based on tumor density with an inset region shown, highlighting the tumor cells (bottom left), cells selected and removed based on tumor contact (bottom middle), and tumor enrichment (bottom right). Scale bars, 100 μm. (**C**) Of all proportions measured, three terms were significantly (Benjamini-Hochberg procedure, $q < 0.05$) associated with early relapse after considering the tumor type. (**D**) Among cell proportions in digital-biopsied spatial areas, four fibroblast-related terms were significantly associated with early relapse (Benjamini-Hochberg procedure, $q < 0.05$). (**E**) After measuring changes between tissues taken from the same patient, digital biopsied terms were significantly associated with early relapse ($P < 0.05$). These terms were primarily immune and fibroblast cells found in immune-, fibroblast-, or epithelial-enriched areas. (**F**) For the percentage of B cells found in fibroblast-enriched areas between patient primary and recurrence samples, the percentage increased in late relapse patients but decreased in early relapse patients.

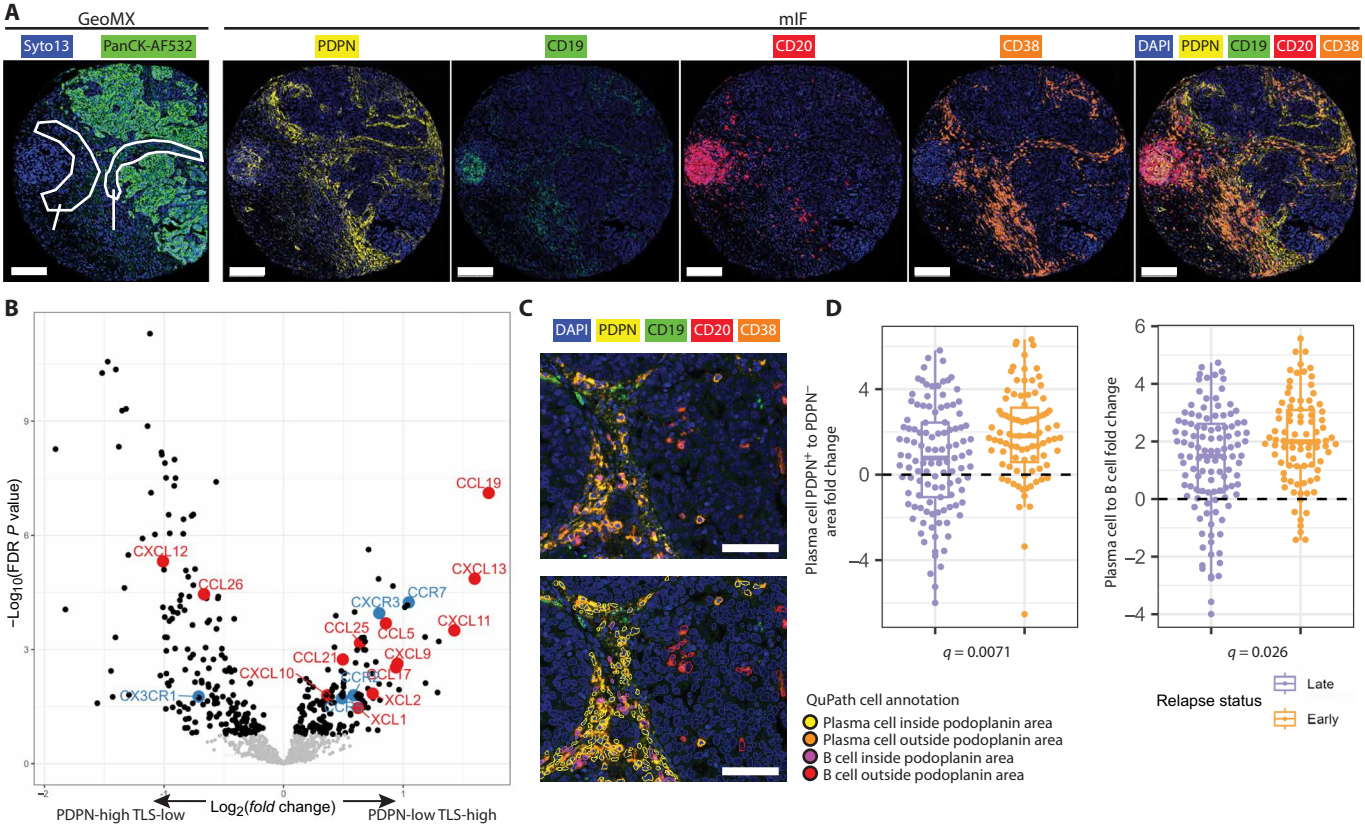

Fig. 5. PDPN and plasma cell spatial analysis. (**A**) Spatial transcriptomic selection of ROIs for digital spatial profiling was aided by multiplex immunofluorescence (mIF) staining with antibodies for PDPN, CD19, CD20, and CD38 ($n = 14$). Most PDPN-positive and PDPN-negative ROIs were in different cores; one core with both types of ROIs is shown for illustration. Scale bars, 200 μm. (**B**) Volcano plot of differential gene expression of ovarian cancer The Cancer Genome Atlas samples stratified by PDPN and TLS gene signature expression (ligands, red; receptors, blue; Benjamini-Hochberg adjustment). (**C**) QuPath AI-aided annotation of plasma cells and B cells located in PDPN-positive and PDPN-negative areas of the tumor. Scale bars, 100 μm. (**D**) Boxplots with scatter plots of the fold change difference of each sample between plasma cells within PDPN-positive areas versus PDPN-negative areas, and plasma cells versus B cells ($q = 0.0071$ and $q = 0.026$, respectively, Wilcoxon rank sum test, Benjamini-Hochberg adjustment).

PDPN-positive areas but not significantly after the Benjamini-Hochberg multi-test correction.

By overlaying human plasma cell and B cell gene signatures defined by Zilionis *et al.* (*60*) onto the heatmap of differentially expressed genes, we noted plasma cell marker (IGKC, MZB1, JCHAIN, XBP1, and IGHG1–4) enrichment in PDPN-positive ROIs, and B cell marker (PAX5 and BANK1) enrichment in PDPN-negative ROIs (fig. S5C). Further exploration of spatial gene expression using Visium digital spatial profiling defined PDPN-positive and PDPN-negative areas in a patient sample. After removal of areas with tumor or endothelial presence leaving 45 PDPN-positive and 18 PDPN-negative 55-μm-diameter immune-infiltrated CAF areas (fig. S5D), we found that plasma cells identified were enriched in PDPN-positive ROIs and that the immune infiltrates in PDPN-positive ROIs were enriched in genes associated with plasma cell differentiation and/or recruitment (JCHAIN, CD38, IGHG3, CD79A, SLAMF7, IGKC, PRDM1, and XBP1; fig. S5E), while the immune infiltrates in PDPN-negative ROIs were enriched in genes typically associated with T and B cells in mature TLSs (CXCL13, MS4A1, CD8A, CD3D, CD3E, CCL19, TRBC1, CD2, CXCL9, and CCR7) (*61*). As an independent validation method for the expression of different cytokines and chemokines and their receptors in PDPN-positive and TLS-positive areas, we stratified patients with ovarian cancer in The Cancer Genome Atlas (TCGA) into $PDPN^{High}$ TLS^{Low} and $PDPN^{Low}$ TLS^{High} based on the expression of PDPN and the TLS gene signature (*62*). The two groups of patients were compared [analysis of variance (ANOVA), Benjamini-Hochberg, $q < 0.01$] to identify differentially expressed CellPhoneDB ligands and receptors (table S5) (*63*). We confirmed that the $PDPN^{Low}$ TLS^{High} tumors were enriched for the chemokine ligands CCL19 and CCL21 and their receptor CCR7 as well as the B cell attractant CXCL13, while the $PDPN^{High}$ TLS^{Low} tumors were enriched for the ligand-receptor pair CCL26-CX3CR1 as well as the plasma cell attractant CXCL12 (Fig. 5B and fig. S5F).

To directly assess potential differences in the spatial organization of CAFs, plasma cells, and B cells between patients experiencing early relapse and late relapse, we performed a targeted spatial analysis of the TMA stained with antibodies against PDPN (predominantly expressed in activated CAFs), CD19 (strongly expressed in B cells and weakly in plasma cells), CD20 (expressed in B cells), and CD38 (expressed in plasma cells). Using QuPath annotation software, we delineated plasma cells and B cells associated with either PDPN-positive or PDPN-negative areas within each sample (Fig. 5C) and calculated the

proportions of each cell subtype relative to all segmented cells in each sample. Samples containing lymph node metastases and those with fewer than five cells of any of the four annotated cell subtypes were excluded from the analysis. By comparing the ratios of the proportions of different cell types (Fig. 5D and fig. S5G), we found that tumors from early relapse patients (<15 months) were significantly more likely to display a higher ratio of plasma cells to B cells ($q = 0.026$), and a higher ratio of plasma cells in PDPN-positive areas compared to PDPN-negative areas ($q = 0.0071$). Collectively, these findings suggest that in early relapse patients, it is more likely that plasma cells are sequestered by CAFs, potentially impeding their contact with cancer cells and other immune cells necessary for an effective immune response.

IMC and H&E measurements are concordant

Next, we compared IMC analysis to standard tools for pathology. Immune cells, fibroblasts, and epithelial cancer cells were phenotyped by morphology in H&E-stained slides using QuPath (fig. S6, A to D). We then compared IMC phenotyping to cell morphology phenotyping. Two H&E sections were phenotyped by morphology, one proximal (~20 μm away from the IMC section) and one distal (~0.8 mm away from the IMC section) (Fig. 6A). We verified that our broad cell types were identified in each of the H&E sections and the IMC section. We found that cell composition in IMC was significantly correlated with the morphology-defined composition (Fig. 6, B to D). This was true for both proximal and distal H&E sections, suggesting that the cell composition was relatively consistent across the tumor. At low cell densities, IMC counts for fibroblasts were lower than H&E morphology counts, and vice versa for epithelial cells (fig. S7A). One challenge in phenotyping by morphology is that immune cells were defined by small round cell morphology, which likely misclassified most macrophages as fibroblasts.

We compared the IHC analysis of whole slides to IMC using a CD8-specific stain to measure the percentage of immune cells that were CD8-positive (Fig. 6E). Generally, the whole slide count was

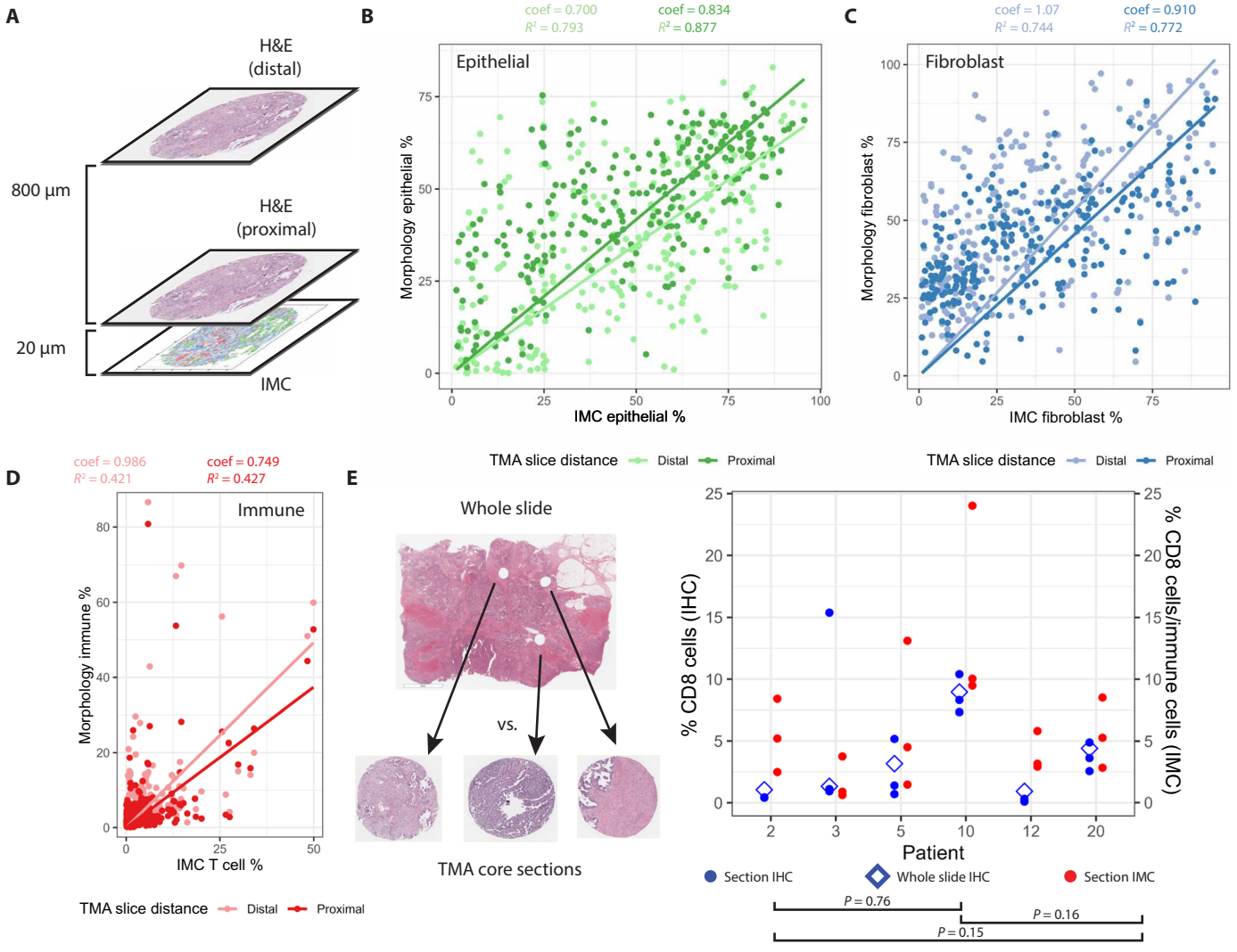

Fig. 6. IMC and pathology comparisons. (**A**) IMC was compared to proximal and distal H&E sections analyzed by cell morphology classification. (**B** to **D**) All IMC cell counts were significantly associated with H&E analysis ($P < 1 \times 10^{-16}$, linear regression). Fibroblast comparisons had the most similar coefficient, while epithelial cell comparisons were the most correlated (R^2). (**E**) For six samples available, three cores were individually analyzed by IMC and proximal H&E slices and compared to the whole image slide (equivalent distance to distal), showing concordance (pairwise *t* test, Benjamini-Hochberg correction).

similar to the counts for individual ROIs, and no statistical differences were observed, although one core from patient 3 proved to be an exception. We further analyzed CD8 T cell composition using multiple methods for a subset of the cohort for which we had transcriptomic data. Using IMC, mIF (analyzed by TissueFAX), IHC (analyzed by QuPath), and spatial gene expression (*64*), we found a high level of correlation across the different methodologies (fig. S7, B to D).

DISCUSSION

Treatment of HGSOC presents a difficult challenge due to the high frequency of late-stage disease at initial diagnosis and the high rate of relapse with platinum-resistant disease following initial tumor debulking surgery and platinum-based chemotherapy. Patients might experience multiple relapses, but despite additional chemotherapy and/or surgery, the remissions typically become progressively shorter, ultimately resulting in treatment-resistant disease. The time to first relapse is a good indicator of tumor aggressiveness and OS (*65*). Using quantitative spatial protein technology, we first confirmed published data about the relevance of immune cells, particularly lymphocytes in TLS-like structures, to patient outcomes (*16*, *47*, *66*). We also performed external validations of our findings, which is essential for highly multiplexed studies, which are processed by automated methods that may be prone to systemic errors. Furthermore, among our observations, we focused on the finding that $PDPN^+$ CAFs were enriched in primary, synchronous metastasis, and recurrence samples from early relapse patients with HGSOC. $PDPN^+$ CAFs have been described as facilitators of immunosuppression and cancer invasion in a variety of solid malignancies [reviewed in (*53*)] and have been associated with disease progression and metastasis in ovarian cancer (*50*, *52*). Here, we used both protein and gene expression spatial analysis to propose that $PDPN^+$ CAFs are more influential and predictive of early relapse in the context of other fibroblasts, as well as B cells and plasma cells.

While single-cell RNA-seq analyses of ovarian carcinomas (*19*, *22*, *23*, *67*–*75*) have confirmed the existence of transcriptomic signatures that define the major cell types previously inferred by bulk transcriptome analyses, those methods have not been able to capture the spatial context of the major cell types within ovarian cancer. Spatial communication between heterogeneous cell types in the tumor microenvironment could affect the efficacy of chemotherapy and immunotherapy, which can be seen in spatial transcriptomic analysis at 50-μm spatial resolution (*35*). Our results show that early relapse is associated with a significant reduction in epithelial cancer cells and increases in fibroblasts in fibroblast-enriched zones. While the observation of a diminished proportion of cancer cells amidst an increased fibroblast population may initially appear paradoxical, it aligns consistently with findings derived from numerous investigations using whole-slide images in large cohorts of patients with ovarian cancer (*76*–*81*). A plausible interpretation of the correlation between early relapse and a lower cancer-fibroblast ratio is that cytotoxic chemotherapy and/or cytotoxic immune cells cannot access cancer cells embedded within the stromal matrix. In preclinical models of solid malignancies, CAFs and CAF-secreted ECM have been shown to reduce immune activity by limiting T cell migration into the tumor area (*19*, *26*, *82*–*86*). In patients with HGSOC treated with standard platinum-based chemotherapy, the immune-excluded phenotype tumors (in which T cells are accumulated in the stroma rather than in the tumor epithelium) had worse survival than the immune-desert phenotype tumors (in which T cells are absent or present in very low numbers), suggesting that the tumor ecosystem and communication between fibroblasts and immune cells are key determinants of clinical outcome (*20*). Our analysis has shown that optimally debulked patients with HGSOC with early and late relapse on standard platinum-based chemotherapy exhibit a distinct spatial configuration of epithelial cancer cells, fibroblasts, and immune cells without significant differences in the overall frequency of the individual cell types. This finding illustrates the advantages spatial analysis of the tumor microenvironment brings to understanding possible causes of early relapse.

As the number of single-cell methodologies has grown, a healthy skepticism has emerged regarding how well single-cell spatial methods can reproduce expert pathology analysis. A major advantage of IMC is the ability to discover cell types expressing combinations of biomarkers due to its information content, which is only possible with highly multiplexed spatial methods. High multiplexity also enables phenotyping via negative selection, where low-expressing cells such as macrophages and myeloid cells are identified by the lack of other marker expression and process of elimination. However, a basic limitation to multiplexed image analysis is that segmentation of single cells remains a challenge, to precisely define cell boundaries without mixing membrane signals from neighboring cells. We encountered this challenge when quantifying CD4/CD8 double-positive and $CD20^+$ T cells, which are increasingly being studied in cancer contexts (*40*–*45*) but may be mistakenly identified in dense-packed tissue. We demonstrated that IMC reproduced many of the features that would be described by a pathologist examining H&E slides and that the IMC-H&E morphology agreement in defining major cell types held true for FFPE tissue section levels up to 1 mm from each other. Thus, the characteristic spatial features of each tumor were relatively consistent over the distance studied (*87*).

Currently, H&E or IHC biomarker assays interpreted by pathologists are the norm in clinical settings, providing the pathologist with a whole-slide perspective and the discretion to isolate or exclude regions based on their relevance to the diagnosis. Because of tumor heterogeneity, using TMA core-sized ROIs (~1 mm^2) instead of whole slides raises concerns of spatial bias that adds uncertainty to statistical correlations between patients and conditions. We used our digital cell biopsies to compare relevant subareas of tissue to mitigate this concern. The spatial analysis revealed that localized immune-epithelial-fibroblast associations have significant associations with early relapse, but the same bulk ROI-wide comparisons do not. The spatial techniques introduced here can be used to add context to the analysis of other studies, for instance, by isolating the tumor cell region of metastatic and recurrent tumors from the host tissue for more accurate deconvolution (*88*). While both the digital biopsies introduced here and spatial niche analysis used broadly in the field (*37*) can be used to identify spatial compartments in tissue, the digital biopsies are mathematically consistent across tissues and experiments, while spatial niches are defined by clustering and are thus less reproducible.

Our study represents a substantial advancement compared to the HGSOC IMC analysis published by Zhu *et al.* (*34*) with respect to the number of patient samples (110 versus 41) and the number of ROIs analyzed (up to triplicates, 257 versus 41). In addition, our patient cohort was relatively homogenous, which allowed for robust comparison of longitudinally collected tumor samples. All 42 patients were optimally debulked (absence of visible residual disease after surgery) and later relapsed with HGSOC. All primary tumors and

synchronous metastases were collected before chemotherapy while all metachronous recurrent metastases were collected after three to six cycles of platinum-based chemotherapy. Notably, our study should not be directly compared to the study by Zhu *et al.* (*34*) due to the different cell subpopulations and different groups of patients analyzed. While the study by Zhu *et al.* (*34*) compared cell densities in primary HGSOC samples from short-term survivors (OS, ≤20 months) and long-term survivors (OS, ≥60 months), we focused on relapse time as the primary clinical endpoint to better characterize patients who should be monitored for signs of relapse and receive more aggressive treatments.

Our findings suggest that B cells and plasma cells are clinically important factors determining a patient's time to relapse. Previous reports have shown conflicting associations between plasma cells and prognosis even within the same cancer type (*89*). In HGSOC, tumor-infiltrating plasma cells were shown to be associated with TLS and better prognosis (*47*, *90*). However, a recent analysis of HGSOC showed that plasma cells correlated with the density of mesenchymal cells and that patients with more plasma cells in their tumors had a significantly shorter survival time than those with fewer plasma cells (*91*). We have developed a unified hypothesis (Fig. 7A) to explain the varying impact of plasma cells on the prognosis of HGSOC. We found that plasma cells were present in two distinct microenvironments, TLS-like lymphoid aggregates and CAFs, within the tumor, which are associated with different prognostic outcomes. In cases where lymphoid aggregates were abundant, plasma cells were linked to a good prognosis possibly because plasma cells were integrated into an organized immunogenic structure that facilitates functional communication between B cells and T cells. Conversely, in cases where CAFs were prevalent, plasma cells were associated with a poor prognosis (*91*), possibly due to the lack of contact with other immune cells.

A hypothesis outlining the mechanism underlying the recruitment of plasma cells by CAFs is depicted in Fig. 7B. TLS FRCs and CAFs share similar expression profiles, including high expression of PDPN (*92*). Lymphoid tissue organization is primarily regulated by the chemotactic activities of chemokines (*93*, *94*), which differ in FRCs and CAFs. The main chemokines associated with FRCs and CAFs are CXCL13 and CXCL12, respectively (*3*, *94*). These chemokines have a selective attraction for B cells and plasma cells, respectively (*95*). Phenotypically, $PDPN^+$ CAFs resemble medullary FRCs, which express PDPN and CXCL12 but not CXCL13 and are involved in plasma cell recruitment and survival (*96*). Studies in genetically modified mice showed that CXCL12 was capable of recruiting lymphoid infiltrates but the infiltrates were malformed, contained few T cells, and were enriched in plasma cells (*95*), which is consistent with independent studies showing that CXCL12 repels T cells (*97*) and attracts plasma cells (*98*). While CXCL13 was included in our panel, the staining did not pass quality control, and further analysis will require optimization of the probes for these chemokines. Generally, the ECM has not been thoroughly profiled using highly multiplexed spatial analyses, making it a prime target for future studies of immune exclusion, nutrient access, and pharmacokinetics in stroma-rich tumors such as HGSOC.

This study emphasizes the need for precise characterization of plasma cell spatial distribution to understand their role in tumor biology, and future studies will analyze larger panels of proteins and more diverse analytes in larger tissue samples as the economics of highly multiplexed analysis becomes more favorable. We hypothesize that bortezomib, an agent that targets plasma cells, may be an effective antitumor therapy in cases where plasma cells are primarily associated with CAFs. Preclinical experimental evidence showed that the depletion of plasma cells by bortezomib reversed the mesenchymal characteristics of ovarian cancer and inhibited in vivo tumor growth (*91*). At present, ClinicalTrials.gov lists a total of eight phase 1 or phase 2 clinical trials in which bortezomib is used in conjunction with various therapeutic approaches for the treatment of patients with HGSOC. The early results from these clinical trials show that only a small subset of patients exhibit partial or complete treatment response, suggesting that further stratification may be needed to improve response rates. The results of our spatial TME analyses indicate that bortezomib has the potential to perturb the spatial arrangement of plasma cells and CAFs, thereby facilitating

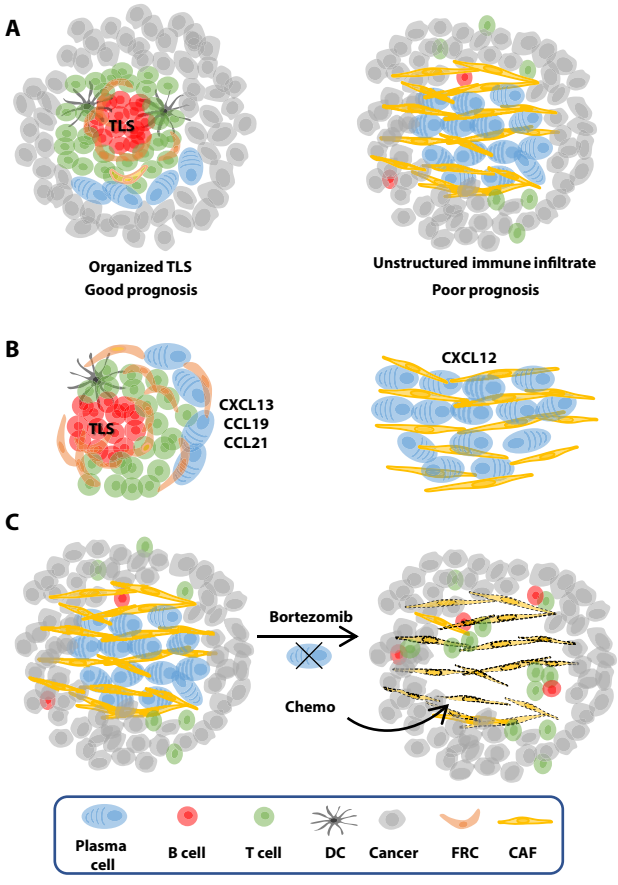

Fig. 7. Proposed spatial importance of B cells, plasma cells, TLS, and CAFs. (**A**) TLS is an organized aggregate of multiple cell types, including immune cells and FRCs, which mediate the interaction between B and T cells to promote differentiation of B cells into plasma cells with antitumor implications. In contrast, plasma cells found within CAFs do not have direct contact with B and T cells to initiate antitumor functions, which may contribute to the negative impact of plasma cells on prognosis in these cases. (**B**) TLS FRCs and CAFs exhibit similar expression profiles; however, FRCs secrete a range of chemokines that attract B cells, whereas CAFs predominantly express CXCL12, which specifically attracts plasma cells. (**C**) Preclinical experiments have shown that depleting plasma cells with bortezomib can reverse the mesenchymal characteristics of ovarian cancer and inhibit tumor growth. Targeting plasma cells with bortezomib has the potential to disrupt the arrangement of CAFs, which could enhance the accessibility of chemotherapy agents to the tumor site.

improved accessibility of chemotherapy agents to the tumor site (Fig. 7C).

MATERIALS AND METHODS

Sample selection

This study was approved by the Cedars-Sinai Institutional Review Board (IRB; Pro44852). All the samples included in this study were obtained from patients who granted their consent for the utilization of their tissue for research purposes. Three types of tumors were collected from 42 patients—primary, synchronous metastatic, and metachronous recurrent tumors. Primary and synchronous metastatic tumors were acquired during primary debulking surgery (pre-chemotherapy), while metachronous/recurrent metastases were acquired during second-look surgery (post-chemotherapy). Primary ovarian tumors were collected from sites including the ovary, fallopian tube, or peritoneum, and synchronous and metachronous/recurrent metastases were collected from various intraperitoneal sites including the omentum, gastrointestinal organs, peritoneum, or lymph node. A histologic diagnosis of HGSOC was confirmed in all tumor samples by pathology. After recovery from primary debulking, surgery all patients were treated with three to six cycles of platinum-based chemotherapy; some were also treated with PARP1 inhibitors after recurrence. All patients in this study relapsed with HGSOC. Some patients had multiple remissions and recurrences. Metadata collected for each patient included the time to first recurrence, OS, age/stage/grade at diagnosis, race, and BRCA mutation status. Clinical and demographic information for the 42 patients is shown in table S1. The average age at diagnosis was 55.4 (range, 45.3 to 62.1) years. Four patients had a prior history of cancer (two breast, one uterine, and one leukemia). The median disease-free interval was 19.6 (range, 5.5 to 51.7) months. Early relapse is heterogeneously defined in the literature (*99*–*101*), we selected 15 months as a cutoff due to the natural distribution of relapse times observed (Fig. 1A). Median OS was 65.9 (range, 15.8 to 156.5) months. Four of 42 patients were alive at the last follow-up (79.6, 91.2, 150.3, and 156.5 months). Forty of the 42 patients were diagnosed with stage III or stage IV disease. Of the two patients diagnosed with stage IIC disease, one was a BRCA1 mutation carrier and one was a BRCA1 and BRCA2 mutation carrier with previous history of breast cancer. Both patients had an aggressive course of the disease. All tumors, except one, were grade 3 serous papillary carcinomas. One patient was diagnosed with stage III, grade 1 to 2 papillary carcinoma arising from a borderline tumor. This patient had four recurrences with the first recurrence at 6.8 months of diagnosis, suggesting rapid differentiation into HGSOC.

Tissue microarray

We define "sample" as tumor tissue obtained from a particular patient's primary, synchronous metastatic, or recurrent metastatic tumor, and "core" as a small circular area excised from a "sample" for further analysis. We generated a TMA with de-identified FFPE patient tissue samples comprising triplicate 1-mm cores of patient-matched primary HGSOC, synchronous pretreatment metastasis, and metachronous posttreatment/recurrent metastasis samples (referred to as primary, synchronous metastasis, and recurrence, respectively) from 42 patients (*102*). Cores were extracted and assembled onto the TMA by manual selection by a histopathologist, comprising representative, tumor cell-rich areas of the samples. Each core was analyzed in full using IMC as a single ROI. Not every patient and time point was analyzed in triplicate due to ROIs either lost from the TMA or without tumor tissue. Manually generated masks were used to exclude folded and/or necrotic tissue areas and staining artifacts. In total, 110 tumor samples (36 primaries, 36 synchronous metastases, and 38 recurrences) and 267 total ROIs were analyzed, for an average of 2.42 ROIs per patient and time point available.

H&E cell morphology phenotyping and immunohistochemistry

H&E-stained TMA slides were digitized (40×) using the Aperio AT Turbo slide scanner from Leica Biosystems. Epithelial cancer cells, fibroblasts, and immune cells were phenotyped by morphology in digitized H&E-stained TMA slides using QuPath software for TMA analysis (TMA DeArrayer) and random trees (RTrees)–trained classifiers (*103*). IHC using the CD8 antibody (clone JCB117, Ventana) was performed by the Cedars-Sinai Medical Center Biobank and Translational Research Core as previously described (*104*). CD8 staining was assessed under the microscope by assigning scores: 0 (absent), 1 (1 to 10%), 2 (11 to 30%), or 3 (>30%) as previously described (*105*) and by QuPath analysis using the positive cell detection tool (*103*). mIF staining was performed by the UCLA Translational Pathology Core Laboratory using tyramide signal amplification. The Opal Polaris 7-Color Automation IHC Kit (catalog no. NEL871001KT, Akoya Biosciences) was used with ER2 30-min retrieval and 1-hour room temperature incubation. Staining was performed consecutively using the following antibodies and dilutions: CD19 [Dako/Agilent, M7296 (1 to 100)], PDPN [Sigma, HPA007534 (1 to 500)], CD38 [Leica, NCL-L-Cd38 (1 to 100)], CD20 [Dako/Agilent, M0755 (1 to 200)], and 4′,6-diamidino-2-phenylindole (Akoya Biosciences, catalog no. SKU FP1490). The slides were scanned at 20× with the Vectra Polaris scanner (Akoya Biosciences) and data from the multispectral camera were analyzed using QuPath software TMA DeArrayer. RTrees was used to train an object classifier to identify five different cell types: CAF-expressing cells, B cells in the PDPN-positive area, plasma cells in the PDPN-positive area, B cells in the PDPN-negative area, and plasma cells in the PDPN-negative area. At least 20 examples were provided to train the classifier. The individual cell types were enumerated and divided by the total number of segmented cells.

IMC sample preparation

De-identified human tonsils and human tumor samples were used to optimize the immunostaining conditions. Antibodies were conjugated using MaxPar kits (Fluidigm/Standard BioTools) or directly purchased in conjugated form. FFPE slides were heated at 60°C for 90 min and then immersed in xylene for 20 min. The slides were then subjected to 100, 95, 80, and 70% ethanol washing steps for 5 min each. After washing with the alcohol gradient, the slides were immersed in tris-EDTA antigen retrieval solution for 30 min at 95°C and then left in the solution for 30 min at room temperature. After the antigen retrieval step, the slides were blocked with 3% bovine serum albumin for 45 min and then stained overnight at 4°C. The next day, the slides were washed twice with PBS with 0.1% Triton X-100 solution and 1× PBS for 8 min each, incubated with 191 iridium (a nuclear stain) for 40 min, washed with distilled water, and then dried before ablation.

Data acquisition and processing

Data were acquired on the Hyperion/Helios Imaging Mass Cytometry platform (Fluidigm/Standard BioTools) at the Cedars Sinai Spatial Molecular Profiling Shared Resource. IMC data were acquired at an acquisition speed of 200 Hz. Single cells were identified using the ilastik random forest pixel classification program. Multiple markers for cell nuclei and membrane/cytosol were used to add redundancy to the classification, and single-cell masks were verified by visual inspection. Artifacts and defects in segmentation, such as folded tissues or necrotic areas, were identified and manually excised from each ROI. Antibodies with poor or nonspecific staining were excluded from the final analysis. Cells were filtered for size and those with an area <15 or >500 μm^2 were removed. The signal for each protein was arcsinh transformed, censored at the 99th percentile, and scaled from 0 to 1. ROIs with fewer than 500 cells total were removed from the analysis, leaving a total of 1,578,369 cells from 267 ROIs for analysis, not including control tissues. Cell phenotypes were obtained using PhenoGraph clustering (k = 15) (*106*) followed by manual annotation.

GeoMx digital spatial profiling analysis

GeoMx (Nanostring, Seattle, WA) digital spatial profiling on the TMA was conducted by the UCLA Technology Center for Genomics & Bioinformatics TCGB. As a guide for ROI selection, nuclei and epithelial cells were labeled using Syto13 and PanCK-AF532 antibodies, respectively. Seven PDPN-positive and seven PDPN-negative areas were selected. The RNA in the ROIs was quantified using NovaSeq SP sequencing (325 to 400 M per lane, Illumina). The counts were mapped to the location in the tissue, resulting in a spatially resolved digital profile of mRNA. Geometric means were used to compare PDPN-positive and PDPN-negative expression ratios.

Visium digital spatial profiling analysis

Publicly available dataset 10X Genomics, Human Ovarian Cancer, 11 mm Capture Area (FFPE), v2, Space Ranger, Visium CytAssist (www.10xgenomics.com/resources/datasets/human-ovarian-cancer-11-mm-capture-area-ffpe-2-standard) and the 10X Genomics Loupe browser were used for the analysis of differential gene expression between PDPN-positive and PDPN-negative Visium ROIs with immune cell infiltrates. ROIs that contained tumor cells or endothelial cells were excluded from the analysis.

Spatial analysis

Multitype nearest neighbor distribution (Gcross) analysis was performed using the spatstat R package. Actual observed and expected nearest neighbor distances between two cell types were calculated, distances were normalized to 50 μm, and the difference between the expected and observed distances was obtained. In a Gcross differential plot between two different cell types A and B, a positive value for the Gcross differential indicates that there are fewer B cells close to A cells than would be expected in a random distribution; thus, the two cell types are segregated in space. A negative differential indicates that the cell types A and B are more intermixed or paired together than a random distribution would predict. A negative A-B differential (B cells are intermixed with A cells) does not necessarily result in a negative B-A differential based on the cell proportions and distribution. For a Gcross differential plot within a single-cell type, A to A, a negative differential denotes cell clustering and a positive differential denotes more regular, distant spacing between cells of type A.

The "digital cell biopsy" method is defined as preselecting specific cells for analysis by a spatial condition. To perform spatial analysis using digital biopsies and to identify lymphoid aggregates, we performed a modified nearest-neighbor analysis. For every cell in each ROI, we calculated an enrichment score based on that cell's proximity to each of the three cell subtypes of interest (immune, epithelial, and fibroblast). The score is calculated by measuring the average distance of each cell to its five nearest neighbors of the specified cell type, capped at 100 μm. The average of these distances is scaled from 0 to 1 by dividing by 100 μm and subtracting from 1, such that 0 indicates minimal interaction between the two cell types. Three primary cell interaction scores—an immune spatial, cancer epithelial spatial, and fibroblast spatial score—are calculated for each cell, as well as interaction scores with immune subtypes such as T cells and macrophages.

TCGA data analysis

The values of the plasma cell gene signature (*60*) and the TLS gene signature (*62*) in the ovarian TCGA dataset were defined as the average z-score of all genes within the signature. Patients with plasma cell signature z-score > 0 (n = 242 patients) were included in the downstream analyses. Two groups of patients were identified based on PDPN expression and TLS z-score: $PDPN^{High}TLS^{Low}$ (PDPN-positive expression value and TLS signature negative z-score, n = 28 patients) and $PDPN^{Low}$ TLS^{High} (PDPN-negative expression value and TLS signature positive z-score, n = 75 patients). Differential gene expression analysis (ANOVA, false discovery rate, q <= 0.01) identified 642 genes differentially expressed genes between the two groups, including 230 receptor-ligand genes listed in CellPhoneDB (*63*).

Modeling and statistics

To test for statistical significance in Gcross differences by early and late relapse status, the glm.cluster function in the R miceadds package was used. For each type of comparison (immune-immune, immune-fibroblast, etc.), the ΔGcross data consisted of the difference between the observed nearest neighbor and the actual difference (y-axis data), measured by the distance from each cell at increments of 1 up to 50 μm (x-axis data). Using the x-axis distance as the clustering variable, we calculated the significance of refractoriness using a generalized linear model to determine whether the spatial tissue composition was significantly associated with refractoriness when considering the tumor type (primary, synchronous metastasis, and recurrence). Multi-test correction using the Benjamini-Hochberg procedure was performed to test the significance of cell proportions toward predicting early relapse. For comparisons within patients across time points, the absolute difference in cell proportions was used and not the relative change, and multi-test correction was not applied due to high variability in the scale of absolute cell differences. All patients were women, and the average age at diagnosis of early and late relapse patients was 56.0 ± 10.8 years and 55.3 ± 8.9 years, respectively. GeoMx terms were filtered for genes with PDPN-positive to PDPN-negative gene expression ratios >1.25 or <0.8, before applying Welch's t test with Benjamini-Hochberg correction. For spatial analysis of mIF, Welch's t test was applied to cell percentage comparisons between ROIs, and the Wilcoxon signed-rank test was applied to cell ratio comparisons, before the Benjamini-Hochberg correction.

Supplementary Materials

This PDF file includes:

Supplementary Methods
Figs. S1 to S7
Tables S1 to S5

REFERENCES AND NOTES

1. D. D. Bowtell, S. Bohm, A. A. Ahmed, P. J. Aspuria, R. C. Bast Jr., V. Beral, J. S. Berek, M. J. Birrer, S. Blagden, M. A. Bookman, J. D. Brenton, K. B. Chiappinelli, F. C. Martins, G. Coukos, R. Drapkin, R. Edmondson, C. Fotopoulou, H. Gabra, J. Galon, C. Gourley, V. Heong, D. G. Huntsman, M. Iwanicki, B. Y. Karlan, A. Kaye, E. Lengyel, D. A. Levine, K. H. Lu, I. A. McNeish, U. Menon, S. A. Narod, B. H. Nelson, K. P. Nephew, P. Pharoah, D. J. Powell Jr., P. Ramos, I. L. Romero, C. L. Scott, A. K. Sood, E. A. Stronach, F. R. Balkwill, Rethinking ovarian cancer II: Reducing mortality from high-grade serous ovarian cancer. *Nat. Rev. Cancer* **15**, 668–679 (2015).
2. M. Kraman, P. J. Bambrough, J. N. Arnold, E. W. Roberts, L. Magiera, J. O. Jones, A. Gopinathan, D. A. Tuveson, D. T. Fearon, Suppression of antitumor immunity by stromal cells expressing fibroblast activation protein-α. *Science* **330**, 827–830 (2010).
3. C. Feig, J. O. Jones, M. Kraman, R. J. B. Wells, A. Deonarine, D. S. Chan, C. M. Connell, E. W. Roberts, Q. Zhao, O. L. Caballero, S. A. Teichmann, T. Janowitz, D. I. Jodrell, D. A. Tuveson, D. T. Fearon, Targeting CXCL12 from FAP-expressing carcinoma-associated fibroblasts synergizes with anti-PD-L1 immunotherapy in pancreatic cancer. *Proc. Natl. Acad. Sci. U.S.A.* **110**, 20212–20217 (2013).
4. V. Cremasco, J. L. Astarita, A. L. Grauel, S. Keerthivasan, K. MacIsaac, M. C. Woodruff, M. Wu, L. Spel, S. Santoro, Z. Amoozgar, T. Laszewski, S. C. Migoni, K. Knoblich, A. L. Fletcher, M. LaFleur, K. W. Wucherpfennig, E. Pure, G. Dranoff, M. C. Carroll, S. J. Turley, FAP delineates heterogeneous and functionally divergent stromal cells in immune-excluded breast tumors. *Cancer Immunol. Res.* **6**, 1472–1485 (2018).
5. A. Tejchman, N. Lamerant-Fayel, J. C. Jacquinet, A. Bielawska-Pohl, K. Mleczko-Sanecka, C. Grillon, S. Chouaib, M. Ugorski, C. Kieda, Tumor hypoxia modulates podoplanin/CCL21 interactions in CCR7+ NK cell recruitment and CCR7+ tumor cell mobilization. *Oncotarget* **8**, 31876–31887 (2017).
6. J. L. Astarita, V. Cremasco, J. Fu, M. C. Darnell, J. R. Peck, J. M. Nieves-Bonilla, K. Song, Y. Kondo, M. C. Woodruff, A. Gogineni, L. Onder, B. Ludewig, R. M. Weimer, M. C. Carroll, D. J. Mooney, L. Xia, S. J. Turley, The CLEC-2-podoplanin axis controls the contractility of fibroblastic reticular cells and lymph node microarchitecture. *Nat. Immunol.* **16**, 75–84 (2015).
7. B. Mlecnik, G. Bindea, H. K. Angell, P. Maby, M. Angelova, D. Tougeron, S. E. Church, L. Lafontaine, M. Fischer, T. Fredriksen, M. Sasso, A. M. Bilocq, A. Kirilovsky, A. C. Obenauf, M. Hamieh, A. Berger, P. Bruneval, J. J. Tuech, J. C. Sabourin, F. Le Pessot, J. Mauillon, A. Rafii, P. Laurent-Puig, M. R. Speicher, Z. Trajanoski, P. Michel, R. Sesboue, T. Frebourg, F. Pages, V. Valge-Archer, J. B. Latouche, J. Galon, Integrative analyses of colorectal cancer show immunoscore is a stronger predictor of patient survival than microsatellite instability. *Immunity* **44**, 698–711 (2016).
8. B. Mlecnik, G. Bindea, A. Kirilovsky, H. K. Angell, A. C. Obenauf, M. Tosolini, S. E. Church, P. Maby, A. Vasaturo, M. Angelova, T. Fredriksen, S. Mauger, M. Waldner, A. Berger, M. R. Speicher, F. Pagès, V. Valge-Archer, J. Galon, The tumor microenvironment and Immunoscore are critical determinants of dissemination to distant metastasis. *Sci. Transl. Med.* **8**, 327ra26 (2016).
9. H. C. Bosmuller, P. Wagner, J. K. Peper, H. Schuster, D. L. Pham, K. Greif, C. Beschorner, H. G. Rammensee, S. Stevanovic, F. Fend, A. Staebler, Combined immunoscore of CD103 and CD3 identifies long-term survivors in high-grade serous ovarian cancer. *Int. J. Gynecol. Cancer* **26**, 671–679 (2016).
10. E. Becht, N. A. Giraldo, C. Germain, A. de Reynies, P. Laurent-Puig, J. Zucman-Rossi, M. C. Dieu-Nosjean, C. Sautes-Fridman, W. H. Fridman, Immune contexture, immunoscore, and malignant cell molecular subgroups for prognostic and theranostic classifications of cancers. *Adv. Immunol.* **130**, 95–190 (2016).
11. H. Angell, J. Galon, From the immune contexture to the Immunoscore: The role of prognostic and predictive immune markers in cancer. *Curr. Opin. Immunol.* **25**, 261–267 (2013).
12. P. A. Ascierto, M. Capone, W. J. Urba, C. B. Bifulco, G. Botti, A. Lugli, F. M. Marincola, G. Ciliberto, J. Galon, B. A. Fox, The additional facet of immunoscore: Immunoprofiling as a possible predictive tool for cancer treatment. *J. Transl. Med.* **11**, 54 (2013).
13. J. Galon, B. Mlecnik, G. Bindea, H. K. Angell, A. Berger, C. Lagorce, A. Lugli, I. Zlobec, A. Hartmann, C. Bifulco, I. D. Nagtegaal, R. Palmqvist, G. V. Masucci, G. Botti, F. Tatangelo, P. Delrio, M. Maio, L. Laghi, F. Grizzi, M. Asslaber, C. D'Arrigo, F. Vidal-Vanaclocha, E. Zavadova, L. Chouchane, P. S. Ohashi, S. Hafezi-Bakhtiari, B. G. Wouters, M. Roehrl, L. Nguyen, Y. Kawakami, S. Hazama, K. Okuno, S. Ogino, P. Gibbs, P. Waring, N. Sato, T. Torigoe, K. Itoh, P. S. Patel, S. N. Shukla, Y. Wang, S. Kopetz, F. A. Sinicrope, V. Scripcariu, P. A. Ascierto, F. M. Marincola, B. A. Fox, F. Pages, Towards the introduction of the 'Immunoscore' in the classification of malignant tumours. *J. Pathol.* **232**, 199–209 (2014).
14. J. Galon, F. Pages, F. M. Marincola, H. K. Angell, M. Thurin, A. Lugli, I. Zlobec, A. Berger, C. Bifulco, G. Botti, F. Tatangelo, C. M. Britten, S. Kreiter, L. Chouchane, P. Delrio, H. Arndt, M. Asslaber, M. Maio, G. V. Masucci, M. Mihm, F. Vidal-Vanaclocha, J. P. Allison, S. Gnjatic, L. Hakansson, C. Huber, H. Singh-Jasuja, C. Ottensmeier, H. Zwierzina, L. Laghi, F. Grizzi, P. S. Ohashi, P. A. Shaw, B. A. Clarke, B. G. Wouters, Y. Kawakami, S. Hazama, K. Okuno, E. Wang, J. O'Donnell-Tormey, C. Lagorce, G. Pawelec, M. I. Nishimura, R. Hawkins, R. Lapointe, A. Lundqvist, S. N. Khleif, S. Ogino, P. Gibbs, P. Waring, N. Sato, T. Torigoe, K. Itoh, P. S. Patel, S. N. Shukla, R. Palmqvist, I. D. Nagtegaal, Y. Wang, C. D'Arrigo, S. Kopetz, F. A. Sinicrope, G. Trinchieri, T. F. Gajewski, P. A. Ascierto, B. A. Fox, Cancer classification using the Immunoscore: A worldwide task force. *J. Transl. Med.* **10**, 205 (2012).
15. A. Kirilovsky, F. Marliot, C. El Sissy, N. Haicheur, J. Galon, F. Pages, Rational bases for the use of the Immunoscore in routine clinical settings as a prognostic and predictive biomarker in cancer patients. *Int. Immunol.* **28**, 373–382 (2016).
16. Ovarian Tumor Tissue Analysis (OTTA) Consortium, E. L. Goode, M. S. Block, K. R. Kalli, R. A. Vierkant, W. Chen, Z. C. Fogarty, A. Gentry-Maharaj, A. Tołoczko, A. Hein, A. L. Bouligny, A. Jensen, A. Osorio, A. Hartkopf, A. Ryan, A. Chudecka-Głaz, A. M. Magliocco, A. Hartmann, A. Y. Jung, B. Gao, B. Y. Hernandez, B. L. Fridley, B. M. McCauley, C. J. Kennedy, C. Wang, C. Karpinskyj, C. B. de Sousa, D. G. Tiezzi, D. L. Wachter, E. Herpel, F. A. Taran, F. Modugno, G. Nelson, J. Lubiński, J. Menkiszak, J. Alsop, J. Lester, J. García-Donas, J. Nation, J. Hung, J. Palacios, J. H. Rothstein, J. L. Kelley, J. M. de Andrade, L. Robles-Díaz, M. P. Intermaggio, M. Widschwendter, M. W. Beckmann, M. Ruebner, M. Jimenez-Linan, N. Singh, O. Oszurek, P. R. Harnett, P. F. Rambau, P. Sinn, P. Wagner, P. Ghatage, R. Sharma, R. P. Edwards, R. B. Ness, S. Orsulic, S. Y. Brucker, S. E. Johnatty, T. A. Longacre, E. Ursula, V. McGuire, W. Sieh, Y. Natanzon, Z. Li, A. S. Whittemore, A. Anna, A. Staebler, B. Y. Karlan, B. Gilks, D. D. Bowtell, E. Høgdall, F. J. Candido dos Reis, H. Steed, I. G. Campbell, J. Gronwald, J. Benítez, J. M. Koziak, J. Chang-Claude, K. B. Moysich, L. E. Kelemen, L. S. Cook, M. T. Goodman, M. J. García, P. A. Fasching, S. Kommoss, S. Deen, S. K. Kjaer, U. Menon, J. D. Brenton, P. D. P. Pharoah, G. Chenevix-Trench, D. G. Huntsman, S. J. Winham, M. Köbel, S. J. Ramus, Dose-response association of $CD8^+$ tumor-infiltrating lymphocytes and survival time in high-grade serous ovarian cancer. *JAMA Oncol.* **3**, e173290 (2017).
17. L. Zhang, J. R. Conejo-Garcia, D. Katsaros, P. A. Gimotty, M. Massobrio, G. Regnani, A. Makrigiannakis, H. Gray, K. Schlienger, M. N. Liebman, S. C. Rubin, G. Coukos, Intratumoral T cells, recurrence, and survival in epithelial ovarian cancer. *N. Engl. J. Med.* **348**, 203–213 (2003).
18. E. Sato, S. H. Olson, J. Ahn, B. Bundy, H. Nishikawa, F. Qian, A. A. Jungbluth, D. Frosina, S. Gnjatic, C. Ambrosone, J. Kepner, T. Odunsi, G. Ritter, S. Lele, Y. T. Chen, H. Ohtani, L. J. Old, K. Odunsi, Intraepithelial $CD8^+$ tumor-infiltrating lymphocytes and a high $CD8^+$/regulatory T cell ratio are associated with favorable prognosis in ovarian cancer. *Proc. Natl. Acad. Sci. U.S.A.* **102**, 18538–18543 (2005).
19. M. Hornburg, M. Desbois, S. Lu, Y. Guan, A. A. Lo, S. Kaufman, A. Elrod, A. Lotstein, T. M. DesRochers, J. L. Munoz-Rodriguez, X. Wang, J. Giltnane, O. Mayba, S. J. Turley, R. Bourgon, A. Daemen, Y. Wang, Single-cell dissection of cellular components and interactions shaping the tumor immune phenotypes in ovarian cancer. *Cancer Cell* **39**, 928–944.e6 (2021).
20. M. Desbois, A. R. Udyavar, L. Ryner, C. Kozlowski, Y. Guan, M. Dürrbaum, S. Lu, J. P. Fortin, H. Koeppen, J. Ziai, C. W. Chang, S. Keerthivasan, M. Plante, R. Bourgon, C. Bais, P. Hegde, A. Daemen, S. Turley, Y. Wang, Integrated digital pathology and transcriptome analysis identifies molecular mediators of T-cell exclusion in ovarian cancer. *Nat. Commun.* **11**, 5583 (2020).
21. U. K. Scarlett, M. R. Rutkowski, A. M. Rauwerdink, J. Fields, X. Escovar-Fadul, J. Baird, J. R. Cubillos-Ruiz, A. C. Jacobs, J. L. Gonzalez, J. Weaver, S. Fiering, J. R. Conejo-Garcia, Ovarian cancer progression is controlled by phenotypic changes in dendritic cells. *J. Exp. Med.* **209**, 495–506 (2012).
22. S. Olalekan, B. Xie, R. Back, H. Eckart, A. Basu, Characterizing the tumor microenvironment of metastatic ovarian cancer by single-cell transcriptomics. *Cell Rep.* **35**, 109165 (2021).
23. B. Izar, I. Tirosh, E. H. Stover, I. Wakiro, M. S. Cuoco, I. Alter, C. Rodman, R. Leeson, M. J. Su, P. Shah, M. Iwanicki, S. R. Walker, A. Kanodia, J. C. Melms, S. Mei, J. R. Lin, C. B. M. Porter, M. Slyper, J. Waldman, L. Jerby-Arnon, O. Ashenberg, T. J. Brinker, C. Mills, M. Rogava, S. Vigneau, P. K. Sorger, L. A. Garraway, P. A. Konstantinopoulos, J. F. Liu, U. Matulonis, B. E. Johnson, O. Rozenblatt-Rosen, A. Rotem, A. Regev, A single-cell landscape of high-grade serous ovarian cancer. *Nat. Med.* **26**, 1271–1279 (2020).
24. E. A. Pietilä, J. Gonzalez-Molina, L. Moyano-Galceran, S. Jamalzadeh, K. Zhang, L. Lehtinen, S. P. Turunen, T. A. Martins, O. Gultekin, T. Lamminen, K. Kaipio, U. Joneborg, J. Hynninen, S. Hietanen, S. Grénman, R. Lehtonen, S. Hautaniemi, O. Carpén, J. W. Carlson, K. Lehti, Co-evolution of matrisome and adaptive adhesion dynamics drives ovarian cancer chemoresistance. *Nat. Commun.* **12**, 3904 (2021).
25. C. Kreuzinger, A. Geroldinger, D. Smeets, E. I. Braicu, J. Sehouli, J. Koller, A. Wolf, S. Darb-Esfahani, K. Joehrens, I. Vergote, A. Vanderstichele, B. Boeckx, D. Lambrechts, H. Gabra, G. B. A. Wisman, F. Trillsch, G. Heinze, R. Horvat, S. Polterauer, E. Berns, C. Theillet, D. Cacsire Castillo-Tong, A complex network of tumor microenvironment in human high-grade serous ovarian cancer. *Clin. Cancer Res.* **23**, 7621–7632 (2017).

26. M. C. W. Westergaard, K. Milne, M. Pedersen, T. Hasselager, L. R. Olsen, M. S. Anglesio, T. H. Borch, M. Kennedy, G. Briggs, S. Ledoux, C. Kreuzinger, I. von der Decken, M. Donia, D. C. Castillo-Tong, B. H. Nelson, I. M. Svane, Changes in the tumor immune microenvironment during disease progression in patients with ovarian cancer. *Cancers* **12**, 3828 (2020).
27. C. Giesen, H. A. O. Wang, D. Schapiro, N. Zivanovic, A. Jacobs, B. Hattendorf, P. J. Schüffler, D. Grolimund, J. M. Buhmann, S. Brandt, Z. Varga, P. J. Wild, D. Günther, B. Bodenmiller, Highly multiplexed imaging of tumor tissues with subcellular resolution by mass cytometry. *Nat. Methods* **11**, 417–422 (2014).
28. M. Angelo, S. C. Bendall, R. Finck, M. B. Hale, C. Hitzman, A. D. Borowsky, R. M. Levenson, J. B. Lowe, S. D. Liu, S. Zhao, Y. Natkunam, G. P. Nolan, Multiplexed ion beam imaging of human breast tumors. *Nat. Med.* **20**, 436–442 (2014).
29. Y. Goltsev, N. Samusik, J. Kennedy-Darling, S. Bhate, M. Hale, G. Vazquez, S. Black, G. P. Nolan, Deep profiling of mouse splenic architecture with CODEX multiplexed imaging. *Cell* **174**, 968–981.e15 (2018).
30. K. Pelka, M. Hofree, J. H. Chen, S. Sarkizova, J. D. Pirl, V. Jorgji, A. Bejnood, D. Dionne, W. H. Ge, K. H. Xu, S. X. Chao, D. R. Zollinger, D. J. Lieb, J. W. Reeves, C. A. Fuhrman, M. L. Hoang, T. Delorey, L. T. Nguyen, J. Waldman, M. Klapholz, I. Wakiro, O. Cohen, J. Albers, C. S. Smillie, M. S. Cuoco, J. Wu, M. J. Su, J. Yeung, B. Vijaykumar, A. M. Magnuson, N. Asinovski, T. Moll, M. N. Goder-Reiser, A. S. Applebaum, L. K. Brais, L. K. DelloStritto, S. L. Denning, S. T. Phillips, E. K. Hill, J. K. Meehan, D. T. Frederick, T. Sharova, A. Kanodia, E. Z. Todres, J. Jané-Valbuena, M. Biton, B. Izar, C. D. Lambden, T. E. Clancy, R. Bleday, N. Melnitchouk, J. Irani, H. Kunitake, D. L. Berger, A. Srivastava, J. L. Hornick, S. Ogino, A. Rotem, S. Vigneau, B. E. Johnson, R. B. Corcoran, A. H. Sharpe, V. K. Kuchroo, K. Ng, M. Giannakis, L. T. Nieman, G. M. Boland, A. J. Aguirre, A. C. Anderson, O. Rozenblatt-Rosen, A. Regev, N. Hacohen, Spatially organized multicellular immune hubs in human colorectal cancer. *Cell* **184**, 4734–4785.e20 (2021).
31. D. Moldoveanu, L. Ramsay, M. Lajoie, L. Anderson-Trocme, M. Lingrand, D. Berry, L. J. M. Perus, Y. Wei, C. Moraes, R. Alkallas, S. Rajkumar, D. Zuo, M. Dankner, E. H. Xu, N. R. Bertos, H. S. Najafabadi, S. Gravel, S. Costantino, M. J. Richer, A. W. Lund, S. V. Del Rincon, A. Spatz, W. H. Miller Jr., R. Jamal, R. Lapointe, A. M. Mes-Masson, S. Turcotte, K. Petrecca, S. Dumitra, A. N. Meguerditchian, K. Richardson, F. Tremblay, B. Wang, M. Chergui, M. C. Guiot, K. Watters, J. Stagg, D. F. Quail, C. Mihalcioiu, S. Meterissian, I. R. Watson, Spatially mapping the immune landscape of melanoma using imaging mass cytometry. *Sci. Immunol.* **7**, eabi5072 (2022).
32. J. S. Nielsen, R. A. Sahota, K. Milne, S. E. Kost, N. J. Nesslinger, P. H. Watson, B. H. Nelson, $CD20^+$ tumor-infiltrating lymphocytes have an atypical $CD27^-$ memory phenotype and together with $CD8^+$ T cells promote favorable prognosis in ovarian cancer. *Clin. Cancer Res.* **18**, 3281–3292 (2012).
33. Y. Zhu, T. L. Yeung, J. Sheng, E. M. Hinchcliff, J. K. Burks, A. A. Jazaeri, S. C. Mok, S. T. C. Wong, An image informatics pipeline for imaging mass cytometry to characterize the immune landscape in pre- and on-treatment immune therapy and its application in recurrent platinium-resistant epithelial ovarian cancer, in *2019 IEEE EMBS International Conference on Biomedical & Health Informatics (BHI)* (IEEE, 2019), pp. 1–4.
34. Y. Zhu, S. Ferri-Borgogno, J. Sheng, T. L. Yeung, J. K. Burks, P. Cappello, A. A. Jazaeri, J. H. Kim, G. H. Han, M. J. Birrer, S. C. Mok, S. T. C. Wong, SIO: A spatioimageomics pipeline to identify prognostic biomarkers associated with the ovarian tumor microenvironment. *Cancers* **13**, 1777 (2021).
35. E. Stur, S. Corvigno, M. Xu, K. Chen, Y. Tan, S. Lee, J. Liu, E. Ricco, D. Kraushaar, P. Castro, J. Zhang, A. K. Sood, Spatially resolved transcriptomics of high-grade serous ovarian carcinoma. *iScience* **25**, 103923 (2022).
36. S. M. Keating, D. L. Taylor, A. L. Plant, E. D. Litwack, P. Kuhn, E. J. Greenspan, C. M. Hartshorn, C. C. Sigman, G. J. Kelloff, D. D. Chang, G. Friberg, J. S. H. Lee, K. Kuida, Opportunities and challenges in implementation of multiparameter single cell analysis platforms for clinical translation. *Clin. Transl. Sci.* **11**, 267–276 (2018).
37. H. W. Jackson, J. R. Fischer, V. R. T. Zanotelli, H. R. Ali, R. Mechera, S. D. Soysal, H. Moch, S. Muenst, Z. Varga, W. P. Weber, B. Bodenmiller, The single-cell pathology landscape of breast cancer. *Nature* **578**, 615–620 (2020).
38. A. W. Zhang, A. McPherson, K. Milne, D. R. Kroeger, P. T. Hamilton, A. Miranda, T. Funnell, N. Little, C. P. E. de Souza, S. Laan, S. LeDoux, D. R. Cochrane, J. L. P. Lim, W. Yang, A. Roth, M. A. Smith, J. Ho, K. Tse, T. Zeng, I. Shlafman, M. R. Mayo, R. Moore, H. Failmezger, A. Heindl, Y. K. Wang, A. Bashashati, D. S. Grewal, S. D. Brown, D. Lai, A. N. C. Wan, C. B. Nielsen, C. Huebner, B. Tessier-Cloutier, M. S. Anglesio, A. Bouchard-Côté, Y. Yuan, W. W. Wasserman, C. B. Gilks, A. N. Karnezis, S. Aparicio, J. N. McAlpine, D. G. Huntsman, R. A. Holt, B. H. Nelson, S. P. Shah, Interfaces of malignant and immunologic clonal dynamics in ovarian cancer. *Cell* **173**, 1755–1769.e22 (2018).
39. T. S. Sumida, K. C. O'Connor, Identity thieves: T cells steal CD20 from B cells but mark themselves for certain death. *Sci. Immunol.* **7**, eabq7242 (2022).
40. M. de Bruyn, V. R. Wiersma, M. C. A. Wouters, D. F. Samplonius, H. G. Klip, W. Helfrich, H. W. Nijman, P. Eggleton, E. Bremer, $CD20^+$ T cells have a predominantly Tc1 effector memory phenotype and are expanded in the ascites of patients with ovarian cancer. *Oncoimmunology* **4**, e999536 (2015).
41. R. Salani, I. Neuberger, R. J. Kurman, R. E. Bristow, H.-W. Chang, T.-L. Wang, L.-M. Shih, Expression of extracellular matrix proteins in ovarian serous tumors. *Int. J. Gynecol. Pathol.* **26**, 141–146 (2007).
42. G. M. Saed, N. M. Fletcher, M. P. Diamond, R. T. Morris, N. Gomez-Lopez, I. Memaj, Novel expression of CD11b in epithelial ovarian cancer: Potential therapeutic target. *Gynecol. Oncol.* **148**, 567–575 (2018).
43. M. Hensler, L. Kasikova, K. Fiser, J. Rakova, P. Skapa, J. Laco, T. Lanickova, L. Pecen, I. Truxova, S. Vosahlikova, I. Moserova, I. Praznovec, V. Drochytek, M. Rehackova, T. Brtnicky, L. Rob, V. Benes, J. Pistolic, L. Sojka, A. Ryska, C. Sautes-Fridman, W. H. Fridman, L. Galluzzi, R. Spisek, J. Fucikova, M2-like macrophages dictate clinically relevant immunosuppression in metastatic ovarian cancer. *J. Immunother. Cancer* **8**, e000979 (2020).
44. S. Barua, P. Fang, A. Sharma, J. Fujimoto, I. Wistuba, A. U. K. Rao, S. H. Lin, Spatial interaction of tumor cells and regulatory T cells correlates with survival in non-small cell lung cancer. *Lung Cancer* **117**, 73–79 (2018).
45. F. Zhou, G. Shayan, S. Sun, X. Huang, X. Chen, K. Wang, Y. Qu, R. Wu, Y. Zhang, Q. Liu, J. Zhang, J. Luo, X. Shi, Y. Liu, B. Liang, Y. X. Li, J. Wang, J. Yi, Spatial architecture of regulatory T-cells correlates with disease progression in patients with nasopharyngeal cancer. *Front. Immunol.* **13**, 1015283 (2022).
46. S. A. Väyrynen, J. Zhang, C. Yuan, J. P. Väyrynen, A. D. Costa, H. Williams, V. Morales-Oyarvide, M. C. Lau, D. A. Rubinson, R. F. Dunne, M. M. Kozak, W. Wang, D. Agostini-Vulaj, M. G. Drage, L. Brais, E. Reilly, O. Rahma, T. Clancy, J. Wang, D. C. Linehan, A. J. Aguirre, C. S. Fuchs, L. M. Coussens, D. T. Chang, A. C. Koong, A. F. Hezel, S. Ogino, J. A. Nowak, B. M. Wolpin, Composition, spatial characteristics, and prognostic significance of myeloid cell infiltration in pancreatic cancer. *Clin. Cancer Res.* **27**, 1069–1081 (2021).
47. D. R. Kroeger, K. Milne, B. H. Nelson, Tumor-infiltrating plasma cells are associated with tertiary lymphoid structures, cytolytic T-cell responses, and superior prognosis in ovarian cancer. *Clin. Cancer Res.* **22**, 3005–3015 (2016).
48. A. I. Bery, H. M. Shepherd, W. Li, A. S. Krupnick, A. E. Gelman, D. Kreisel, Role of tertiary lymphoid organs in the regulation of immune responses in the periphery. *Cell. Mol. Life Sci.* **79**, 359 (2022).
49. T. Aoki, A. Jiang, A. Xu, Y. Yin, A. Gamboa, K. Milne, K. Takata, T. Miyata-Takata, S. Chung, S. Rai, S. Wu, M. Warren, C. Strong, T. Goodyear, K. Morris, L. C. Chong, M. Hav, A. R. Colombo, A. Telenius, M. Boyle, S. Ben-Neriah, M. Power, A. S. Gerrie, A. P. Weng, A. Karsan, A. Roth, P. Farinha, D. W. Scott, K. J. Savage, B. H. Nelson, A. Merchant, C. Steidl, Spatially resolved tumor microenvironment predicts treatment outcomes in relapsed/refractory hodgkin lymphoma. *J. Clin. Oncol.* **42**, 1077–1087 (2023).
50. I. M. Cobec, I. Sas, L. Pirtea, A. M. Cimpean, A. E. Moatar, R. A. Ceauşu, M. Raica, Podoplanin as key player of tumor progression and lymph vessel proliferation in ovarian cancer. *Anticancer Res* **36**, 5265–5272 (2016).
51. J. L. Astarita, S. E. Acton, S. J. Turley, Podoplanin: Emerging functions in development, the immune system, and cancer. *Front. Immunol.* **3**, 283 (2012).
52. J. R. Varghese, D. S. Gurusamy, S. Kalyanasundaram, S. Kalyanaraman, Role of podoplanin, E-cadherin, Ki-67 in the dissemination of tumor cells in ovarian surface epithelial carcinoma-An immunohistochemical study. *Ann. Diagn. Pathol.* **60**, 151984 (2022).
53. B. Pula, W. Witkiewicz, P. Dziegiel, M. Podhorska-Okolow, Significance of podoplanin expression in cancer-associated fibroblasts: A comprehensive review. *Int. J. Oncol.* **42**, 1849–1857 (2013).
54. A. Kawase, G. Ishii, K. Nagai, T. Ito, T. Nagano, Y. Murata, T. Hishida, M. Nishimura, J. Yoshida, K. Suzuki, A. Ochiai, Podoplanin expression by cancer associated fibroblasts predicts poor prognosis of lung adenocarcinoma. *Int. J. Cancer* **123**, 1053–1059 (2008).
55. Y. Tanaka, T. Ohno, T. Kadonaga, Y. Kidokoro, M. Wakahara, K. Nosaka, T. Sakabe, Y. Suzuki, H. Nakamura, Y. Umekita, Podoplanin expression in cancer-associated fibroblasts predicts unfavorable prognosis in node-negative breast cancer patients with hormone receptor-positive/HER2-negative subtype. *Breast Cancer* **28**, 822–828 (2021).
56. G. Hu, K. Zhong, W. Chen, S. Wang, L. Huang, Podoplanin-positive cancer-associated fibroblasts predict poor prognosis in lung cancer patients. *Onco Targets Ther.* **11**, 5607–5619 (2018).
57. S. E. Acton, J. L. Astarita, D. Malhotra, V. Lukacs-Kornek, B. Franz, P. R. Hess, Z. Jakus, M. Kuligowski, A. L. Fletcher, K. G. Elpek, A. Bellemare-Pelletier, L. Sceats, E. D. Reynoso, S. F. Gonzalez, D. B. Graham, J. Chang, A. Peters, M. Woodruff, Y. A. Kim, W. Swat, T. Morita, V. Kuchroo, M. C. Carroll, M. L. Kahn, K. W. Wucherpfennig, S. J. Turley, Podoplanin-rich stromal networks induce dendritic cell motility via activation of the C-type lectin receptor CLEC-2. *Immunity* **37**, 276–289 (2012).
58. J. Suzuki, K. Aokage, S. Neri, T. Sakai, H. Hashimoto, Y. Su, S. Yamazaki, H. Nakamura, K. Tane, T. Miyoshi, M. Sugano, M. Kojima, S. Fujii, T. Kuwata, A. Ochiai, M. Tsuboi, G. Ishii, Relationship between podoplanin-expressing cancer-associated fibroblasts and the immune microenvironment of early lung squamous cell carcinoma. *Lung Cancer* **153**, 1–10 (2021).
59. D. W. Huang, B. T. Sherman, Q. Tan, J. R. Collins, W. G. Alvord, J. Roayaei, R. Stephens, M. W. Baseler, H. C. Lane, R. A. Lempicki, The DAVID gene functional classification tool: A

novel biological module-centric algorithm to functionally analyze large gene lists. *Genome Biol.* **8**, R183 (2007).
60. R. Zilionis, C. Engblom, C. Pfirschke, V. Savova, D. Zemmour, H. D. Saatcioglu, I. Krishnan, G. Maroni, C. V. Meyerovitz, C. M. Kerwin, S. Choi, W. G. Richards, A. De Rienzo, D. G. Tenen, R. Bueno, E. Levantini, M. J. Pittet, A. M. Klein, Single-cell transcriptomics of human and mouse lung cancers reveals conserved myeloid populations across individuals and species. *Immunity* **50**, 1317–1334.e10 (2019).
61. Y. Hou, S. Qiao, M. Li, X. Han, X. Wei, Y. Pang, H. Mao, The gene signature of tertiary lymphoid structures within ovarian cancer predicts the prognosis and immunotherapy benefit. *Front. Genet.* **13**, 1090640 (2022).
62. M. C. Dieu-Nosjean, J. Goc, N. A. Giraldo, C. Sautes-Fridman, W. H. Fridman, Tertiary lymphoid structures in cancer and beyond. *Trends Immunol.* **35**, 571–580 (2014).
63. M. Efremova, M. Vento-Tormo, S. A. Teichmann, R. Vento-Tormo, CellPhoneDB: Inferring cell-cell communication from combined expression of multi-subunit ligand-receptor complexes. *Nat. Protoc.* **15**, 1484–1506 (2020).
64. A. Talhouk, J. George, C. Wang, T. Budden, T. Z. Tan, D. S. Chiu, S. Kommoss, H. S. Leong, S. Chen, M. P. Intermaggio, B. Gilks, T. M. Nazeran, M. Volchek, W. Elatre, R. C. Bentley, J. Senz, A. Lum, V. Chow, H. Sudderuddin, R. Mackenzie, S. C. Y. Leong, G. Liu, D. Johnson, B. Chen, Aocs Group, J. Alsop, S. N. Banerjee, S. Behrens, C. Bodelon, A. H. Brand, L. Brinton, M. E. Carney, Y.-E. Chiew, K. L. Cushing-Haugen, C. Cybulski, D. Ennis, S. Fereday, R. T. Fortner, J. García-Donas, A. Gentry-Maharaj, R. Glasspool, T. Goranova, C. S. Greene, P. Haluska, H. R. Harris, J. Hendley, B. Y. Hernandez, E. Herpel, M. Jimenez-Linan, C. Karpinskyj, S. H. Kaufmann, G. L. Keeney, C. J. Kennedy, M. Köbel, J. M. Koziak, M. C. Larson, J. Lester, L.-A. Lewsley, J. Lissowska, J. Lubiński, H. Luk, G. Macintyre, S. Mahner, I. A. McNeish, J. Menkiszak, N. Nevins, A. Osorio, O. Oszurek, J. Palacios, S. Hinsley, C. L. Pearce, M. C. Pike, A. M. Piskorz, I. Ray-Coquard, V. Rhenius, C. Rodriguez-Antona, R. Sharma, M. E. Sherman, D. De Silva, N. Singh, P. Sinn, D. Slamon, H. Song, H. Steed, E. A. Stronach, P. J. Thompson, A. Tołoczko, B. Trabert, N. Traficante, C.-C. Tseng, M. Widschwendter, L. R. Wilkens, S. J. Winham, B. Winterhoff, A. Beeghly-Fadiel, J. Benitez, A. Berchuck, J. D. Brenton, R. Brown, J. Chang-Claude, G. Chenevix-Trench, A. deFazio, P. A. Fasching, M. J. García, S. A. Gayther, M. T. Goodman, J. Gronwald, M. J. Henderson, B. Y. Karlan, L. E. Kelemen, U. Menon, S. Orsulic, P. D. P. Pharoah, N. Wentzensen, A. H. Wu, J. M. Schildkraut, M. A. Rossing, G. E. Konecny, D. G. Huntsman, R. Y.-J. Huang, E. L. Goode, S. J. Ramus, J. A. Doherty, D. D. Bowtell, M. S. Anglesio, Development and validation of the gene expression predictor of high-grade serous ovarian carcinoma molecular subTYPE (PrOTYPE). *Clin. Cancer Res.* **26**, 5411–5423 (2020).
65. K. Ushijima, Treatment for recurrent ovarian cancer-at first relapse. *J. Oncol.* **2010**, 497429 (2010).
66. J. Hamanishi, M. Mandai, M. Iwasaki, T. Okazaki, Y. Tanaka, K. Yamaguchi, T. Higuchi, H. Yagi, K. Takakura, N. Minato, T. Honjo, S. Fujii, Programmed cell death 1 ligand 1 and tumor-infiltrating $CD8^+$ T lymphocytes are prognostic factors of human ovarian cancer. *Proc. Natl. Acad. Sci. U.S.A.* **104**, 3360–3365 (2007).
67. Q. Hao, J. Li, Q. Zhang, F. Xu, B. Xie, H. Lu, X. Wu, X. Zhou, Single-cell transcriptomes reveal heterogeneity of high-grade serous ovarian carcinoma. *Clin. Transl. Med.* **11**, e500 (2021).
68. S. Olbrecht, P. Busschaert, J. Qian, A. Vanderstichele, L. Loverix, T. Van Gorp, E. Van Nieuwenhuysen, S. Han, A. Van den Broeck, A. Coosemans, A. S. Van Rompuy, D. Lambrechts, I. Vergote, High-grade serous tubo-ovarian cancer refined with single-cell RNA sequencing: Specific cell subtypes influence survival and determine molecular subtype classification. *Genome Med.* **13**, 111 (2021).
69. K. Zhang, E. P. Erkan, S. Jamalzadeh, J. Dai, N. Andersson, K. Kaipio, T. Lamminen, N. Mansuri, K. Huhtinen, O. Carpén, S. Hietanen, J. Oikkonen, J. Hynninen, A. Virtanen, A. Häkkinen, S. Hautaniemi, A. Vähärautio, Longitudinal single-cell RNA-seq analysis reveals stress-promoted chemoresistance in metastatic ovarian cancer. *Sci. Adv.* **8**, eabm1831 (2022).
70. T. Kan, S. Zhang, S. Zhou, Y. Zhang, Y. Zhao, Y. Gao, T. Zhang, F. Gao, X. Wang, L. Zhao, M. Yang, Single-cell RNA-seq recognized the initiator of epithelial ovarian cancer recurrence. *Oncogene* **41**, 895–906 (2022).
71. B. J. Winterhoff, M. Maile, A. K. Mitra, A. Sebe, M. Bazzaro, M. A. Geller, J. E. Abrahante, M. Klein, R. Hellweg, S. A. Mullany, K. Beckman, J. Daniel, T. K. Starr, Single cell sequencing reveals heterogeneity within ovarian cancer epithelium and cancer associated stromal cells. *Gynecol. Oncol.* **144**, 598–606 (2017).
72. I.-M. Launonen, N. Lyytikäinen, J. Casado, E. A. Anttila, A. Szabó, U.-M. Haltia, C. A. Jacobson, J. R. Lin, Z. Maliga, B. E. Howitt, K. C. Strickland, S. Santagata, K. Elias, A. D. D'Andrea, P. A. Konstantinopoulos, P. K. Sorger, A. Färkkilä, Single-cell tumor-immune microenvironment of BRCA1/2 mutated high-grade serous ovarian cancer. *Nat. Commun.* **13**, 835 (2022).
73. C. M. Laumont, M. C. A. Wouters, J. Smazynski, N. S. Gierc, E. A. Chavez, L. C. Chong, S. Thornton, K. Milne, J. R. Webb, C. Steidl, B. H. Nelson, Single-cell profiles and prognostic impact of tumor-infiltrating lymphocytes coexpressing CD39, CD103, and PD-1 in ovarian cancer. *Clin. Cancer Res.* **27**, 4089–4100 (2021).
74. A. J. Shih, A. Menzin, J. Whyte, J. Lovecchio, A. Liew, H. Khalili, T. Bhuiya, P. K. Gregersen, A. T. Lee, Identification of grade and origin specific cell populations in serous epithelial ovarian cancer by single cell RNA-seq. *PLOS One* **13**, e0206785 (2018).
75. J. Xu, Y. Fang, K. Chen, S. Li, S. Tang, Y. Ren, Y. Cen, W. Fei, B. Zhang, Y. Shen, W. Lu, Single-cell RNA sequencing reveals the tissue architecture in human high-grade serous ovarian cancer. *Clin. Cancer Res.* **28**, 3590–3602 (2022).
76. E. Lou, V. Clemente, M. Grube, A. Svedbom, A. C. Nelson, F. Blome, A. Staebler, S. Kommoss, M. Bazzaro, Tumor-stroma proportion to predict chemoresistance in patients with ovarian cancer. *JAMA Netw. Open* **7**, e240407 (2024).
77. E. Lou, R. I. Vogel, S. Hoostal, M. Klein, M. A. Linden, D. Teoh, M. A. Geller, Tumor-Stroma proportion as a predictive biomarker of resistance to platinum-based chemotherapy in patients with ovarian cancer. *JAMA Oncol.* **5**, 1222–1224 (2019).
78. C. Lan, J. Li, X. Huang, A. Heindl, Y. Wang, S. Yan, Y. Yuan, Stromal cell ratio based on automated image analysis as a predictor for platinum-resistant recurrent ovarian cancer. *BMC Cancer* **19**, 159 (2019).
79. C. Lan, A. Heindl, X. Huang, S. Xi, S. Banerjee, J. Liu, Y. Yuan, Quantitative histology analysis of the ovarian tumour microenvironment. *Sci. Rep.* **5**, 16317 (2015).
80. Y. Chen, L. Zhang, W. Liu, X. Liu, Prognostic significance of the tumor-stroma ratio in epithelial ovarian cancer. *Biomed. Res. Int.* **2015**, 589301 (2015).
81. J. Jiang, B. Tekin, L. Yuan, S. Armasu, S. J. Winham, E. L. Goode, H. Liu, Y. Huang, R. Guo, C. Wang, Computational tumor stroma reaction evaluation led to novel prognosis-associated fibrosis and molecular signature discoveries in high-grade serous ovarian carcinoma. *Front. Med.* **9**, 994467 (2022).
82. H. Salmon, K. Franciszkiewicz, D. Damotte, M. C. Dieu-Nosjean, P. Validire, A. Trautmann, F. Mami-Chouaib, E. Donnadieu, Matrix architecture defines the preferential localization and migration of T cells into the stroma of human lung tumors. *J. Clin. Invest.* **122**, 899–910 (2012).
83. N. Hartmann, N. A. Giese, T. Giese, I. Poschke, R. Offringa, J. Werner, E. Ryschich, Prevailing role of contact guidance in intrastromal T-cell trapping in human pancreatic cancer. *Clin. Cancer Res.* **20**, 3422–3433 (2014).
84. A. Chakravarthy, L. Khan, N. P. Bensler, P. Bose, D. D. De Carvalho, TGF-β-associated extracellular matrix genes link cancer-associated fibroblasts to immune evasion and immunotherapy failure. *Nat. Commun.* **9**, 4692 (2018).
85. S. Mariathasan, S. J. Turley, D. Nickles, A. Castiglioni, K. Yuen, Y. Wang, E. E. Kadel III, H. Koeppen, J. L. Astarita, R. Cubas, S. Jhunjhunwala, R. Banchereau, Y. Yang, Y. Guan, C. Chalouni, J. Ziai, Y. Senbabaoglu, S. Santoro, D. Sheinson, J. Hung, J. M. Giltnane, A. A. Pierce, K. Mesh, S. Lianoglou, J. Riegler, R. A. D. Carano, P. Eriksson, M. Hoglund, L. Somarriba, D. L. Halligan, M. S. van der Heijden, Y. Loriot, J. E. Rosenberg, L. Fong, I. Mellman, D. S. Chen, M. Green, C. Derleth, G. D. Fine, P. S. Hegde, R. Bourgon, T. Powles, TGFβ attenuates tumour response to PD-L1 blockade by contributing to exclusion of T cells. *Nature* **554**, 544–548 (2018).
86. J. A. Grout, P. Sirven, A. M. Leader, S. Maskey, E. Hector, I. Puisieux, F. Steffan, E. Cheng, N. Tung, M. Maurin, R. Vaineau, L. Karpf, M. Plaud, A. L. Begue, K. Ganesh, J. Mesple, M. Casanova-Acebes, A. Tabachnikova, S. Keerthivasan, A. Lansky, J. Le Berichel, L. Walker, A. H. Rahman, S. Gnjatic, N. Girard, M. Lefevre, D. Damotte, J. Adam, J. C. Martin, A. Wolf, R. M. Flores, M. B. Beasley, R. Pradhan, S. Muller, T. U. Marron, S. J. Turley, M. Merad, E. Kenigsberg, H. Salmon, Spatial positioning and matrix programs of cancer-associated fibroblasts promote T cell exclusion in human lung tumors. *Cancer Discov.* **12**, 2606–2625 (2022).
87. P. Kündig, C. Giesen, H. Jackson, B. Bodenmiller, B. Papassotirolopus, S. N. Freiberger, C. Aquino, L. Opitz, Z. Varga, Limited utility of tissue micro-arrays in detecting intra-tumoral heterogeneity in stem cell characteristics and tumor progression markers in breast cancer. *J. Transl. Med.* **16**, 118 (2018).
88. D. R. Robinson, Y. M. Wu, R. J. Lonigro, P. Vats, E. Cobain, J. Everett, X. Cao, E. Rabban, C. Kumar-Sinha, V. Raymond, S. Schuetze, A. Alva, J. Siddiqui, R. Chugh, F. Worden, M. M. Zalupski, J. Innis, R. J. Mody, S. A. Tomlins, D. Lucas, L. H. Baker, N. Ramnath, A. F. Schott, D. F. Hayes, J. Vijai, K. Offit, E. M. Stoffel, J. S. Roberts, D. C. Smith, L. P. Kunju, M. Talpaz, M. Cieślik, A. M. Chinnaiyan, Integrative clinical genomics of metastatic cancer. *Nature* **548**, 297–303 (2017).
89. M. C. A. Wouters, B. H. Nelson, Prognostic significance of tumor-infiltrating b cells and plasma cells in human cancer. *Clin. Cancer Res.* **24**, 6125–6135 (2018).
90. S. Lundgren, J. Berntsson, B. Nodin, P. Micke, K. Jirstrom, Prognostic impact of tumour-associated B cells and plasma cells in epithelial ovarian cancer. *J. Ovarian Res.* **9**, 21 (2016).
91. Z. Yang, W. Wang, L. Zhao, X. Wang, R. C. Gimple, L. Xu, Y. Wang, J. N. Rich, S. Zhou, Plasma cells shape the mesenchymal identity of ovarian cancers through transfer of exosome-derived microRNAs. *Sci. Adv.* **7**, eabb0737 (2021).
92. A. L. Fletcher, S. E. Acton, K. Knoblich, Lymph node fibroblastic reticular cells in health and disease. *Nat. Rev. Immunol.* **15**, 350–361 (2015).
93. L. Tiberio, A. Del Prete, T. Schioppa, F. Sozio, D. Bosisio, S. Sozzani, Chemokine and chemotactic signals in dendritic cell migration. *Cell. Mol. Immunol.* **15**, 346–352 (2018).

94. K. M. Ansel, V. N. Ngo, P. L. Hyman, S. A. Luther, R. Forster, J. D. Sedgwick, J. L. Browning, M. Lipp, J. G. Cyster, A chemokine-driven positive feedback loop organizes lymphoid follicles. *Nature* **406**, 309–314 (2000).
95. S. A. Luther, A. Bidgol, D. C. Hargreaves, A. Schmidt, Y. Xu, J. Paniyadi, M. Matloubian, J. G. Cyster, Differing activities of homeostatic chemokines CCL19, CCL21, and CXCL12 in lymphocyte and dendritic cell recruitment and lymphoid neogenesis. *J. Immunol.* **169**, 424–433 (2002).
96. C. Mionnet, I. Mondor, A. Jorquera, M. Loosveld, J. Maurizio, M. L. Arcangeli, N. H. Ruddle, J. Nowak, M. Aurrand-Lions, H. Luche, M. Bajenoff, Identification of a new stromal cell type involved in the regulation of inflamed B cell follicles. *PLoS Biol.* **11**, e1001672 (2013).
97. M. C. Poznansky, I. T. Olszak, R. Foxall, R. H. Evans, A. D. Luster, D. T. Scadden, Active movement of T cells away from a chemokine. *Nat. Med.* **6**, 543–548 (2000).
98. D. C. Hargreaves, P. L. Hyman, T. T. Lu, V. N. Ngo, A. Bidgol, G. Suzuki, Y. R. Zou, D. R. Littman, J. G. Cyster, A coordinated change in chemokine responsiveness guides plasma cell movements. *J. Exp. Med.* **194**, 45–56 (2001).
99. S. A. Said, R. W. Bretveld, H. Koffijberg, G. S. Sonke, R. F. P. M. Kruitwagen, J. A. de Hullu, A. M. van Altena, S. Siesling, M. A. van der Aa, Clinicopathologic predictors of early relapse in advanced epithelial ovarian cancer: Development of prediction models using nationwide data. *Cancer Epidemiol.* **75**, 102008 (2021).
100. F. Vidal, P. Guerby, M. Luyckx, P. Haddad, E. Stoeckle, P. Morice, E. Leblanc, F. Lecuru, E. Daraï, J. M. Classe, C. Pomel, T. Filleron, G. Ferron, D. Querleu, A. Rafii, Are early relapses in advanced-stage ovarian cancer doomed to a poor prognosis? *PLOS One* **11**, e0147787 (2016).
101. J. J. Han, M. Yu, N. Houston, S. M. Steinberg, E. C. Kohn, Progranulin is a potential prognostic biomarker in advanced epithelial ovarian cancers. *Gynecol. Oncol.* **120**, 5–10 (2011).
102. Y. Hu, M. S. Recouvreux, M. Haro, E. Taylan, B. Taylor-Harding, A. E. Walts, B. Y. Karlan, S. Orsulic, INHBA(+) cancer-associated fibroblasts generate an immunosuppressive tumor microenvironment in ovarian cancer. *NPJ Precis. Oncol.* **8**, 35 (2024).
103. P. Bankhead, M. B. Loughrey, J. A. Fernandez, Y. Dombrowski, D. G. McArt, P. D. Dunne, S. McQuaid, R. T. Gray, L. J. Murray, H. G. Coleman, J. A. James, M. Salto-Tellez, P. W. Hamilton, QuPath: Open source software for digital pathology image analysis. *Sci. Rep.* **7**, 16878 (2017).
104. D. Jia, Z. Liu, N. Deng, T. Z. Tan, R. Y.-J. Huang, B. Taylor-Harding, D.-J. Cheon, K. Lawrenson, W. R. Wiedemeyer, A. E. Walts, B. Y. Karlan, S. Orsulic, A COL11A1-correlated pan-cancer gene signature of activated fibroblasts for the prioritization of therapeutic targets. *Cancer Lett.* **382**, 203–214 (2016).
105. D. J. Cheon, A. E. Walts, J. A. Beach, J. Lester, J. S. Bomalaski, C. S. Walsh, W. Ruprecht Wiedemeyer, B. Y. Karlan, S. Orsulic, Differential expression of argininosuccinate synthetase in serous and non-serous ovarian carcinomas. *J. Pathol. Clin. Res.* **1**, 41–53 (2015).
106. J. H. Levine, E. F. Simonds, S. C. Bendall, K. L. Davis, E.-A. D. Amir, M. D. Tadmor, O. Litvin, H. G. Fienberg, A. Jager, E. R. Zunder, R. Finck, A. L. Gedman, I. Radtke, J. R. Downing, D. Pe'er, G. P. Nolan, Data-driven phenotypic dissection of AML reveals progenitor-like cells that correlate with prognosis. *Cell* **162**, 184–197 (2015).

Acknowledgments: We thank the patients and their families for support of this research. IMC was performed at the Cedars Sinai Spatial Molecular Profiling Shared Resource. GeoMx was performed at the UCLA Technology Center for Genomics and Bioinformatics. mIF was performed at the UCLA Translational Pathology Core Laboratory. **Funding:** S.O. was supported by the NIH grant R01 CA208753, the United States Department of Veterans Affairs Merit Awards VA-ORD I01 BX004974 and I01 BX006020, the Office of the Assistant Secretary of Defense for Health Affairs through the Ovarian Cancer Research Program Award No. W81XWH2210631, and the Sandy Rollman Ovarian Cancer Foundation. S.O. and A.M.X. were supported by the NIH National Center for Advancing Translational Science (NCATS) UCLA CTSI Grant Number UL1TR001881. **Author Contributions:** A.M.X.: Methodology, software, formal analysis, investigation, writing, and visualization. M.H.: Investigation and data curation. A.E.W.: Resources, data curation, and writing (review and editing). Y.H.: Investigation and data curation. J.J.: Investigation. B.Y.K.: Resources and data curation. A.M.: Conceptualization, resources, writing (review and editing), supervision, and project administration. S.O.: Conceptualization, resources, data curation, writing (review and editing), supervision, project administration, and funding acquisition. **Competing interests:** The authors declare that they have no competing interests. **Data and materials availability:** All data needed to evaluate the conclusions of the paper are present in the paper and/or the Supplementary Materials. IMC and GeoMx raw data are available at Zenodo at 10.5281/zenodo.7618945. Analysis scripts and methods are available on request. Analysis was performed using R version 4.2.1 and Rstudio 2022.07.1. Rstudio packages Rcpp, Rphenograph, data.table, tidyverse, gridExtra, pheatmap, uwot, spatstat, viridis, tidyr, stringi, parallel, doParallel, EBImage, ggplot2, ggbeeswarm, miceadds, plotly, and RColorBrewer were used. Images were generated using MCD Viewer (Fluidigm/Standard BioTools). IHC and mIF analyses were performed using QuPath in which cell type classifiers were trained using RandomTrees.

Submitted 17 September 2023
Accepted 15 March 2024
Published 17 April 2024
10.1126/sciadv.adk8805